Nationaal Lucht- en Ruimtevaartlaboratorium

National Aerospace Laboratory NLR

NLR-TR-NLR-TR-2015-218

Spherical harmonics based aggregation in the multilevel fast multipole algorithm

MSc Thesis

S. Hack

Customer	NLR
Contract number	----
Owner	NLR
Division	Aerospace Vehicles
Distribution	
Classification of title	Unclassified
	June 2015

Approved by:

Author	Reviewer	Managing department

Contents

Abstract

Electromagnetic scattering problems arise in a variety of applications, such as radar-cross section computations. In a simplified model, the scatterer is seen as a conductor, with an electric field that is zero inside. An incident radar wave induces a fictitious current on the surface of the scatterer, which cancels the incident wave. The current satisfies a boundary integral equation, which is derived from the Maxwell equations.

Discretization using the boundary element method results in a dense system matrix, because every pair of basis functions interacts through the Green's function for the vector Helmholtz equation. The system matrix is too large even to be stored in the computer's memory for realistic radar frequencies. In 1987, Rokhlin and Greengard proposed the fast multipole method (FMM) [15], which has been named as one of the top ten algorithms of the twentieth century [10]. The matrix-vector products in the Krylov subspace iterations are computed with complexity $O(N \log N)$, rather than in $O(N^2)$ for dense matrix-vector multiplication, where N is the number of unknowns. The physical interpretation of the FMM is based on the fact that the electric field outside a current distribution can be reconstructed from the far field using a multipole expansion in spherical waves propagating outwards. The interactions between basis functions can then be computed in clusters. This results in a factorization of the system matrix, where only the factors are stored, and applied sequentially in the matrix-vector products in the Krylov-subspace method.

In the multilevel fast multipole algorithm (MLFMA), interactions are computed in clusters of varying sizes depending on the distance of the basis functions. The spectral content of the far field increases with the size of the cluster. For large clusters, it is sampled at many directions, and this is expensive to do directly. The key step in the MLFMA therefore is aggregation, where the far field of a large cluster is interpolated from the far fields of its (smaller) sub-clusters. This process is repeated until only the far fields of very small clusters need to be sampled directly.

We present a variant of the multilevel fast multipole algorithm (MLFMA) where the far field radiation patterns are represented in spherical harmonics during aggregation. This allows a reduction in the sample rate by a factor of up to eight. An innovation is the use the real spherical harmonics, which results in CPU time savings. At the levels with large clusters, we intend to switch to Lagrange interpolation because it can be parallellized over the clusters. The preliminary test results indicate that the accuracy is similar to the customary Lagrange interpolation, and that the CPU times are reduced significantly at least at the levels with small clusters.

1 Introduction

Electromagnetic scattering problems arise in a variety of applications, such as radar-cross section computations. The radar-cross section (RCS) of an object is a measure of its visibility on a radar system, and it is of great importance for fighter aircraft. The RCS can be measured experimentally, or predicted by computational models for the scattering of electromagnetic waves. In these models, the object is seen as a metallic conductor or a dielectric medium. In most cases the Maxwell equations in the region surrounding the object are reformulated as an integral equation over the surface of the object, involving the Green's function for the vector Helmholtz equation. Discretisation using boundary elements results in a system of linear equations, which is solved using Krylov subspace methods. The system matrix is dense and the number of nonzero entries scales like $O(N^2)$, where N is the number of unknowns. Unfortunately, for realistic radar frequencies the system matrix is too large even to be stored in the computer's memory.
In 1987, Rokhlin and Greengard proposed the fast multipole method [15] for the Laplace equation. In the following years the underlying ideas were extended to the Helmholtz equation with the multilevel fast multipole algorithm, in which the matrix-vector products in the Krylov-subspace iterations are computed with complexity $O(N \log N)$, rather than in $O(N^2)$ for dense matrix-vector multiplication.
In the fast multipole method, the interactions between the basis functions are not computed individually, but in clusters. The key step is an approximate factorization of the Green's function for the Helmholtz equation by multipole and plane wave expansions, so that element i of the output vector in the matrix-vector product can be expressed as an integral over the surface of the unit sphere

$$\int_{\hat{S}} h_{i,c_1}(\hat{\mathbf{k}}) \sum_{c_2} g_{c_1 c_2}(\hat{\mathbf{k}}) f_{c_2}(\hat{\mathbf{k}}) d\hat{\mathbf{k}}, \tag{1}$$

with $h_{i,c_1}(\hat{\mathbf{k}})$ the sensitivity of basis function i in cluster c_1 to the electromagnetic field, $g_{c_1 c_2}(\hat{\mathbf{k}})$ the transfer function between clusters c_2 and c_1, and $f_{c_2}(\hat{\mathbf{k}})$ the angular dependence of the electromagnetic far field of cluster c_2. Following [8], we will call $f_{c_2}(\hat{\mathbf{k}})$ the far field radiation pattern. It is computed by summation over the far field radiation patterns of the individual basis functions, which are interpreted as current sources and multiplied by the elements of the input vector. The transfer function $g_{c_1 c_2}(\hat{\mathbf{k}})$ contains a truncated multipole expansion and for a fixed number of multipoles the accuracy of the above factorization increases as the distance between the clusters increases.
In the multilevel fast multipole algorithm (MLFMA), interactions are computed in clusters of varying sizes depending on the distance of the basis functions. In computer implementations, the

integral in (1) is computed numerically, and the far field radiation pattern is sampled at the integration points $\hat{\mathbf{k}}_i$. Following [8], we will call the integration points $\hat{\mathbf{k}}_i$ directions in the context of sampling the far field radiation pattern. Furthermore, following [13], the samples of the far field radiation pattern at the directions will be called k-space samples. The required number of k-space samples depends on the spectral content of the far field radiation pattern $f_{c_2}(\hat{\mathbf{k}})$, which increases with the size of a cluster. Directly sampling the far field radiation pattern involves evaluating an integral over the surface of the scatterer, and this is expensive to do for very many directions.

The k-space samples of a large cluster are therefore computed in a process called aggregation. The cluster is subdivided into child clusters. These are smaller, and the spectral content of their far field radiation patterns is also smaller. The child clusters can then be represented by a smaller number of k-space samples. We then employ interpolation to approximately evaluate their far field radiation patterns at the larger number of directions of the parent cluster. The k-space samples of the parent cluster are then obtained by summation over the k-space samples of the child clusters at each direction.

An important feature of far field radiation patterns is that they are defined with respect to some coordinate system. The spectral content of a far field radiation pattern is smallest if the origin of the coordinate system is close to the center of the cluster. It is hence important to shift the origin of the coordinate system of the far field radiation patterns during aggregation.

The above process can also be recursively applied to the child clusters. We then obtain a multilevel structure, where the far field radiation patterns are only directly sampled at the finest level, where each cluster contains about 10 basis functions.

The standard method in the literature is to use Lagrange interpolation, and to apply the shift directly to the k-space samples,

$$e^{\mathrm{i}k\mathbf{k}_i\cdot\mathbf{d}} f(\hat{\mathbf{k}}_i), \tag{2}$$

with $\mathbf{d}$ the distance of the shift. The Lagrange interpolator is a local interpolator, which means that the interpolated function value at the target point is calculated using only the stored k-space samples at a few nearby directions. In contrast, global interpolators use all k-space samples. Local interpolators have an important advantage:

- They can be parallellized over the directions. Global interpolation methods can only be parallellized over the clusters, and at the higher levels the number of clusters is small, severely limiting the number of parallel processes.

Local interpolators also have two disadvantages:

- An interpolation error is incurred if a local interpolator is used. For sufficient accuracy the far field radiation patterns need to be oversampled during the aggregation phase. The

number of directions during the aggregation phase in fact equals the number of integration points that is required for accurate numerical integration of (1), and the transfer function $g_{c_1c_2}(\hat{\mathbf{k}})$ in the integrand has a larger spectral content than the far field radiation pattern. Global interpolators are exact for exactly bandlimited functions if sufficient k-space samples are used.

- The interpolation matrices are sparse, which is disadvantageous for computer implementations. For an equivalent number of nonzero entries, it is preferable to have a small, dense matrix, rather than a large, sparse one.

The aim of this research is to examine an alternative scheme with a much lower sample rate for the aggregation of far field radiation patterns. In this scheme, the far field radiation pattern is represented by its coefficients with respect to the spherical harmonics, which are the analog on the surface of the unit sphere of the Fourier basis functions in 1D. The current research is inspired by the work of Eibert [13] who stored the far field radiation patterns at the finest (with the smallest clusters) level in spherical harmonics, rather than k-space samples. His motivation is to reduce the memory requirements of the MLFMA. In the algorithm presented in this report, the far field radiation patterns are also represented by spherical harmonics at the higher (with larger clusters) levels. The effect of a shift on the spherical harmonics coefficients of a far field radiation pattern is computed directly, and the k-space samples are only reconstructed for the application of the transfer function $g_{c_1c_2}(\hat{\mathbf{k}})$. An arbitrary shift can be decomposed into a rotation, a shift along the z-axis, and the inverse rotation, which results in a computational complexity of $O(K^{\frac{3}{2}})$, with K the sample rate, in this case the number of spherical harmonics coefficients. This decomposition is also used in the different context of the low-frequency multilevel fast multipole algorithm [34]. Following [18], we will call this the RCR-decomposition, where R stands for rotation and C stands for coaxial translation. A further innovation is use of the real spherical harmonics, which is advantageous for the efficiency of the implementation. To our knowledge, the real spherical harmonics have not been used before in the aggregation phase of the MLFMA.
The motivation for the present strategy is that sample rate is reduced by a factor of up to eight compared to the standard method. It is expected that this will result in lower CPU times. The disadvantage of the new scheme is that its computational complexity $O(K^{\frac{3}{2}})$ is higher than for Lagrange interpolation $O(K)$ (with K the number of k-space samples), and other global interpolators that have $O(K \log \sqrt{K})$. In radar-cross section computations, K has values in the range $O(10^1)$ to $O(10^6)$. The new scheme is also expected to be suitable for efficient implementations. The matrices in the RCR decomposition are block diagonal with small and dense blocks, whereas Lagrange interpolation is based on large and sparse matrices. We expect that, for small clusters, the low sample rate (of the order $O(10^2)$ or $O(10^3)$) will make the technique more ef-

ficient. At the higher levels, where the clusters increase in size, it is better to switch to Lagrange interpolation for its smaller computational complexity and better parallellization capabilities. The new scheme is a global interpolator and a bandlimited function is reproduced exactly if sufficient spherical harmonics are used. Far field radiation patterns are not exactly bandlimited, and the interpolation error decays exponentially with the number of spherical harmonics, rather than linearly with the number of k-space samples in Lagrange interpolation. If a low sample rate with few spherical harmonics is used, then the interpolation error is of comparable size to Lagrange interpolators.

To our knowledge, this is the study where the use of spherical harmonics expansions in the aggregation phase of the MLFMA as a means of reducing the sample rate is worked out in detail, including an examination of the error due to the shifts and CPU time measurements where we compare the scheme to Lagrange interpolation. Other schemes in the literature for reducing the sample rate in the aggregation phase of the MLFMA are based on trigonometric polynomial expansions and the fast Fourier transform [31], [6], [22], [23]. These schemes also result in a reduction of the sample rate by a factor of eight, but this reduction is only achieved for large clusters, where we intend to switch to Lagrange interpolation with parallellization over the directions.

The structure of this report is as follows. In Chapters 2-4 we give a summary of scattering problems, the weak formulation and the numerical discretization. In Chapter 5 we describe the fast multipole method as a starting point for our discussion of the standard MLFMA in Chapter 6. In Chapter 7 we describe the use of spherical harmonics coefficients as a representation of the far field radiation patterns at the finest level in the MLFMA. This technique was introduced as a means of saving memory in [13] and the algorithm presented in this report can be seen in some ways as an extension of this technique to the higher levels. In Chapter 8 we discuss the use of spherical harmonics expansions at the higher levels, including the RCR decomposition. In Chapter 9 we provide CPU time measurements and memory estimates. In Chapter 10 the possibilities for extensions of the algorithm to reduce the computational complexity are discussed. Finally, we conclude with a discussion of our results in Chapter 11.

2 Scattering problems

In this chapter scattering problems are described. The visibility of an aircraft (or another object like a bird) on a radar system is measured by its radar-cross section, which is computed for a given time-harmonic incident electric field

$$\boldsymbol{E}^{\text{inc}}(\boldsymbol{r},t) = \boldsymbol{E}^{\text{inc}}(\boldsymbol{r})e^{\mathrm{i}\omega t}, \tag{3}$$

representing ground-based and aircraft-mounted radar systems. Radar-cross section computations are based on the electric field integral equation (EFIE), which is derived in [7]. Define the operator

$$\boldsymbol{L}(\boldsymbol{X}) = ik\left(\int_S \boldsymbol{X}(\boldsymbol{r}')\phi(\boldsymbol{r},\boldsymbol{r}') - \frac{1}{k^2}(\nabla'\cdot\boldsymbol{X}(\boldsymbol{r}'))\nabla'\phi(\boldsymbol{r},\boldsymbol{r}')d\boldsymbol{r}'\right)_t, \tag{4}$$

with $(\cdot)_t$ the tangential part, S the scatterer, $k = \omega/c$ the spatial frequency, ω the angular frequency, c the speed of light, ∇' the gradient with respect to the integration variable $\boldsymbol{r}'$, $\boldsymbol{r}$ the field variable, and ϕ the Green's function

$$\phi(\boldsymbol{r},\boldsymbol{r}') = \frac{e^{-\mathrm{i}k|\boldsymbol{r}-\boldsymbol{r}'|}}{|\boldsymbol{r}-\boldsymbol{r}'|}. \tag{5}$$

The scatterer S is the boundary $\partial\Omega$ of the region Ω surrounding the scatterer. Let the impedance in free space be given by

$$\eta = \sqrt{\frac{\mu_0}{\epsilon_0}}, \tag{6}$$

with ε_0 and μ_0 the free-space dielectric constant and permittivity, respectively. The scatterer is modeled as a perfect electric conductor, with a fictitious surface-current $\boldsymbol{J}_s$ that completely cancels the incident electric field. The EFIE is given by

$$\eta\boldsymbol{L}(\boldsymbol{J}_s) = 4\pi\boldsymbol{E}_t^{\text{inc}}. \tag{7}$$

The operator $\boldsymbol{L}$ can be interpreted as the electric field generated by a current distribution $\boldsymbol{J}_s$ multiplied by the constant $-\frac{4\pi}{\eta}$. The scattering problem consists of computing the current $\boldsymbol{J}_s$ given an incident electric field $\boldsymbol{E}^{\text{inc}}$. The radar-cross section can be computed using $\boldsymbol{J}_s$. The operator $\boldsymbol{L}$ is singular and at certain resonance frequencies there are nonzero $\boldsymbol{J}_s$ solutions for a zero $\boldsymbol{E}^{\text{inc}}$. These solutions are nonphysical and can be avoided by also examining the magnetic field integral equation and solving a combined field integral equation. The EFIE is sufficient to explain the fast multipole method and will be considered in this report. An important feature of RCS computations is that they are repeated for many different angles of the incident field. Therefore only the solution phase of the algorithm discussed in this report needs to be efficient, and not the initialization phase.

3 Weak formulation

In this chapter the weak formulation of the EFIE is given. Define the following two bilinear operators

$$\begin{aligned}\mathcal{L}_1(\boldsymbol{X}, \boldsymbol{Y}) &= \int_S \int_S \phi(\boldsymbol{r}, \boldsymbol{r}') \boldsymbol{X}(\boldsymbol{r}') \cdot \boldsymbol{Y}(\boldsymbol{r}) d\boldsymbol{r}' d\boldsymbol{r}, \\ \mathcal{L}_2(\boldsymbol{X}, \boldsymbol{Y}) &= \int_S \int_S (\nabla' \cdot \boldsymbol{X}(\boldsymbol{r}')) \phi(\boldsymbol{r}, \boldsymbol{r}') (\nabla \cdot \boldsymbol{Y}(\boldsymbol{r})) d\boldsymbol{r}' d\boldsymbol{r}.\end{aligned}$$

Let $\boldsymbol{W}$ be a test-vector field that is tangential to the surface, and that is an element of $H^{-\frac{1}{2}}(\mathrm{div})$, the space of vector functions f for which

$$\int_S \int_S \frac{f(\boldsymbol{r}) \cdot \overline{f(\boldsymbol{r}')}}{R} d\boldsymbol{r}' d\boldsymbol{r} + \int_S \int_S \frac{\nabla \cdot f(\boldsymbol{r}) \overline{\nabla' \cdot f(\boldsymbol{r}')}}{R} d\boldsymbol{r}' d\boldsymbol{r}$$

is finite. This function space follows from the trace theorem in functional analysis and the assumption that the electric field and its divergence have finite energy, in other words, that they are locally square integrable. Details can be found in [21]. The tangential trial-vector field $\boldsymbol{J}_s$ is also an element of $H^{-\frac{1}{2}}(\mathrm{div})$. The weak formulation is then given by

$$\int_S 4\pi \, \boldsymbol{W} \cdot \boldsymbol{E}_t^{\mathrm{inc}} d\boldsymbol{r} = \mathrm{i}k\eta(\mathcal{L}_1(\boldsymbol{W}, \boldsymbol{J}_s) - \frac{1}{k^2}\mathcal{L}_2(\boldsymbol{W}, \boldsymbol{J}_s)). \tag{8}$$

Again, the details can be found in [21].

4 Discretisation

The RWG basis functions from Rao, Wilton and Glisson [29] are used on a piecewise linear approximation of the surface with triangular elements. These basis functions are defined for each edge, that is not on the boundary of the surface (in the case that it is not closed)

$$\mathbf{f}_j(\mathbf{r}) = \begin{cases} \pm \dfrac{l}{A^{\pm}}(\mathbf{r} - \mathbf{r}^{\pm}) & \mathbf{r} \in T^{\pm} \\ \mathbf{0} & \text{elsewhere} \end{cases}, \tag{9}$$

with $T^{\pm}$ the two triangles incident to the edge, l the length of the edge, $A^{\pm}$ the areas of the triangles and $\mathbf{r}^{\pm}$ the corner points opposite the edge. The basis functions are illustrated in Figure 1. The current $\mathbf{J}_s$ is approximated as a linear combination of N basis functions

$$\mathbf{J}_s = \sum_{j=1}^{N} J_j \mathbf{f}_j. \tag{10}$$

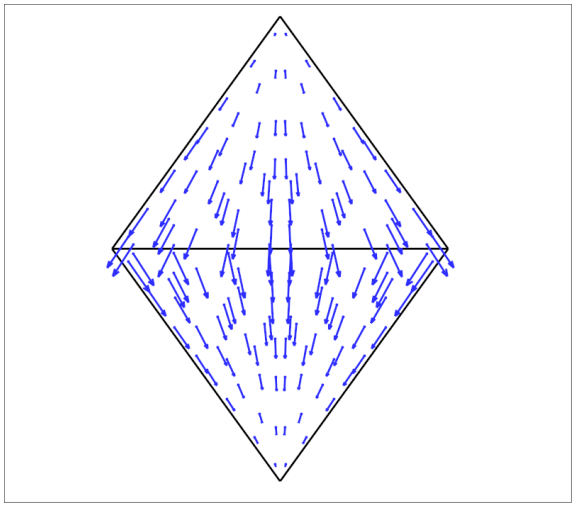

Fig. 1 RWG basis function

For the test functions the same basis elements are used. The following linear system is then found

$$\int_S \boldsymbol{f}_i \cdot 4\pi \boldsymbol{E}_t^{\text{inc}} d\boldsymbol{r} = \sum_{j=1}^{N} \eta \mathcal{L}_{ij} J_j, \quad , i = 1, \ldots, N, \tag{11}$$

with

$$\mathcal{L}_{ij} = \mathcal{L}(\boldsymbol{f}_i, \boldsymbol{f}_j), \tag{12}$$

and

$$\mathcal{L} = \mathrm{i}k(\mathcal{L}_1 + \frac{1}{k^2}\mathcal{L}_2). \tag{13}$$

5 Fast multipole method

In this chapter the fast multipole method is described. The linear system (11) is solved using a Krylov iterative method, in which the system matrix is required only for matrix-vector products. It can be seen that the system matrix is full, and that the complexity of the matrix-vector products is therefore $O(N^2)$. For radar-cross section computations with a realistic size the system matrix is too large even to be stored in memory. The fast multipole method (FMM) improves the CPU and memory requirements to $O(N\sqrt{N})$.

In Section 5.1 the fast multipole method is derived using multipole and plane wave expansions of the Green's function for the Helmholtz equation. In this section we give an alternative derivation

of the fast multipole method with the goal of clarifying the physics behind it. The entries of the system matrix are given by

$$\mathcal{L}_{ij} = \int_S \mathbf{f}_i(\boldsymbol{r}) \cdot \frac{-4\pi}{\eta}[\mathbf{E}(\mathbf{f}_j)](\boldsymbol{r}) d\boldsymbol{r}, \tag{14}$$

which express the interaction of the electric field $\mathbf{E}(\mathbf{f}_j)$ induced by the source current $\mathbf{f}_j$ with the basis function $\mathbf{f}_i$. The basis function related to the test function is interpreted as the sensitivity at $\boldsymbol{r}$ of the surface to the electric field. Note that the basis functions are seen as scatterers in their own right. The fast multipole method is based on the idea that the electric field outside a current distribution can be reconstructed from the electromagnetic far field [11]. Recall that in scattering problems we seek solutions to the Helmholtz equation

$$\nabla^2 \mathbf{E}(\mathbf{r}) + k^2 \mathbf{E}(\mathbf{r}) = \mathbf{0}. \tag{15}$$

We will solve the Helmholtz equation in the exterior of $B(\mathbf{0}, d)$, the sphere centered in $\mathbf{0}$, with radius d chosen so that the source current $\mathbf{f}_j$ is contained inside. In scattering problems it is conventional to apply the Sommerfeld radiation condition, see [24] for a discussion. If this condition is applied, then the electric field has the following multipole expansion outside the sphere

$$\mathbf{E}(r\hat{\mathbf{r}}) = \sum_{p=0}^{\infty} \sum_{q=-p}^{p} \mathbf{E}_{pq} h_p^{(2)}(kr) Y_p^q(\hat{\mathbf{r}}), \tag{16}$$

with $\hat{\mathbf{r}}$ the unit vector in the direction of $\mathbf{r}$, $r = |\mathbf{r}|$, $\mathbf{E}_{pq}$ the spherical harmonics coefficients of the electric field, $h_p^{(2)}$ the spherical Hankel function of the second kind, and $Y_p^q(\hat{\mathbf{r}})$ the spherical harmonics, given in spherical coordinates by

$$Y_p^q(\theta, \phi) := (-1)^q \left[\frac{(p-q)!}{(p+q)!} \frac{2p+1}{4\pi} \right]^{1/2} P_p^q(\cos(\theta)) e^{\mathrm{i}q\phi},$$

with p the degree, q the order, and P_p^q the associated Legendre polynomial of degree p and order q. See [3] for details about the special functions. The spherical harmonics are illustrated in Figure 2. The spherical harmonics can be seen as the analog on the unit sphere of the Fourier components in 1D. A key property of the spherical harmonics is that they are an orthonormal basis for functions on the unit sphere in the L^2-inner product. The terms $\mathbf{E}_{pq} h_p^{(2)}(kr) Y_p^q(\hat{\mathbf{r}})$ are spherical waves propagating outward. In the above discussion, all the components of the electric field have been represented by separate multipole expansions. The components are decoupled in the Helmholtz equation, but the electric field actually has additional structure. The radial component of the radiated electric field decays to zero as $r \to \infty$. Fewer expansion coefficients are required if the spherical vector harmonics are used instead of the Y_p^q. This will make the analysis more complicated though, and we do not pursue this topic. Details can be found in [24]. Solutions to

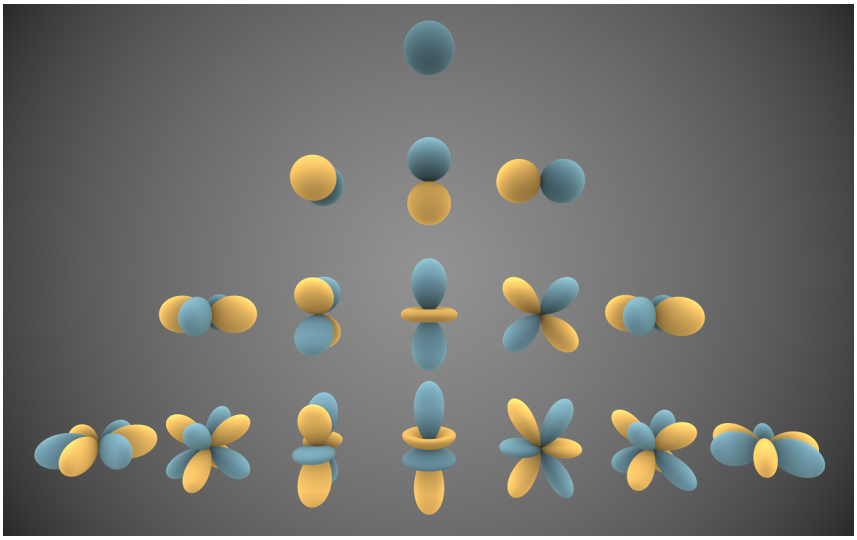

Fig. 2 real spherical harmonics (73). *They are ordered by degree from top to bottom and by order from left to right. Blue regions indicate where the functions are positive. The distance from the origin indicates the magnitude. Figure from Inigo.quilez. 14 May 2014 via* `http://commons.wikimedia.org/wiki/File:Spherical_Harmonics.png`, *Creative Commons Attribution-Share Alike 3.0 Unported*

the Helmholtz equation due to a bounded current distribution have a limit in the far field $r \to \infty$, given by [5]

$$\mathbf{E}(r\hat{\mathbf{r}}) = (\mathbb{I} - \hat{\boldsymbol{r}}\hat{\boldsymbol{r}})\frac{-\mathrm{i}ke^{-\mathrm{i}kr}}{4\pi r}\int_S \mathbf{f}_j(\boldsymbol{r}')e^{\mathrm{i}k\boldsymbol{r}'\cdot\hat{\mathbf{r}}}d\mathbf{r}', \quad r \to \infty, \tag{17}$$

with $(\mathbb{I} - \hat{\boldsymbol{r}}\hat{\boldsymbol{r}})$ the projection operator

$$\boldsymbol{v} \mapsto \boldsymbol{v} - (\hat{\boldsymbol{r}} \cdot \boldsymbol{v})\hat{\boldsymbol{r}}. \tag{18}$$

The angular dependence $(\mathbb{I} - \hat{\boldsymbol{r}}\hat{\boldsymbol{r}})\int_S \mathbf{f}_j(\boldsymbol{r}')e^{\mathrm{i}k\boldsymbol{r}'\cdot\hat{\mathbf{r}}}d\mathbf{r}'$ is called the far field radiation pattern. They are also sometimes called outgoing waves in the literature, because the terms in the multipole expansion $\mathbf{E}_{pq}h_p^{(2)}(kr)Y_p^q(\hat{\mathbf{r}})$ are spherical waves propagating outward. The spherical Hankel functions of the second kind have the following limit behavior

$$h_p^{(2)}(kr) \to \frac{(\mathrm{i})^{p+1}e^{-\mathrm{i}kr}}{kr}, \tag{19}$$

as $r \to \infty$. By taking the limit as $r \to \infty$ in (16), and equating it to (17), we can reconstruct the spherical harmonics coefficients of the electric field

$$\mathbf{E}_{pq} = \frac{-k^2}{4\pi(\mathrm{i})^p}\int_{\hat{S}}(\mathbb{I} - \hat{\boldsymbol{k}}\hat{\boldsymbol{k}})\int_S \mathbf{f}_j(\mathbf{r}')e^{\mathrm{i}k\boldsymbol{r}'\cdot\hat{\mathbf{k}}}d\boldsymbol{r}'Y_p^{q*}(\hat{\mathbf{k}})d\hat{\mathbf{k}}, \tag{20}$$

with $\hat{S}$ the unit sphere (not to be confused with the complement of the domain in which we are solving the Helmholtz equation), $(\cdot)^*$ the complex conjugate, and where we have used the notation $\hat{\mathbf{k}}$ instead of $\hat{\mathbf{r}}$. The $\hat{\mathbf{k}}$ are called directions in [8]. Following [13], integrals over the surface of the unit sphere are called k-space integrals. The electric field is then given by

$$\mathbf{E}(r\hat{\mathbf{r}}) = \sum_{p=0}^{\infty}\sum_{q=-p}^{p} h_p^{(2)}(kr)Y_p^q(\hat{\mathbf{r}})\frac{-k^2}{4\pi(\mathrm{i})^p}\int_{\hat{S}}(\mathbb{I}-\hat{\boldsymbol{k}}\hat{\boldsymbol{k}})\int_S \mathbf{f}_j(\mathbf{r}')e^{\mathrm{i}k\boldsymbol{r}'\cdot\hat{\mathbf{k}}}d\boldsymbol{r}'Y_p^{q*}(\hat{\mathbf{k}})d\hat{\mathbf{k}}. \tag{21}$$

We absorb the summation over the order into the k-space integral over $\hat{S}$

$$\mathbf{E}(r\hat{\mathbf{r}}) = \sum_{p=0}^{\infty} h_p^{(2)}(kr)\frac{-k^2}{4\pi(\mathrm{i})^p}\int_{\hat{S}}(\mathbb{I}-\hat{\boldsymbol{k}}\hat{\boldsymbol{k}})\int_S \mathbf{f}_j(\mathbf{r}')e^{\mathrm{i}k\boldsymbol{r}'\cdot\hat{\mathbf{k}}}d\boldsymbol{r}'\sum_{q=-p}^{p} Y_p^q(\hat{\mathbf{r}})Y_p^{q*}(\hat{\mathbf{k}})d\hat{\mathbf{k}}. \tag{22}$$

Spherical harmonics of degree p are homogeneous polynomials of degree p. The set of homogeneous polynomials of degree p is invariant under a rotation. Therefore, spherical harmonics in the spherical coordinate system where the North pole matches the vector $\hat{\mathbf{r}}$ can be expressed as a linear combination of spherical harmonics in the Cartesian coordinate system, where the North pole matches the vector $\mathbf{e}_z$. In fact, we have for the spherical harmonic with order zero in the rotated coordinate system that

$$\frac{2p+1}{4\pi}P_p(\hat{\mathbf{k}}\cdot\hat{\mathbf{r}}) = \sum_{q=-p}^{p} Y_p^q(\hat{\mathbf{p}})Y_p^{q*}(\hat{\mathbf{k}}), \tag{23}$$

with P_p the Legendre polynomial of degree p. See [3] for details about the special functions. We then find for the electric field

$$\mathbf{E}(r\hat{\mathbf{r}}) = \sum_{p=0}^{\infty} h_p^{(2)}(kr)\frac{-k^2(2p+1)}{(4\pi)^2(\mathrm{i})^p}\int_{\hat{S}}(\mathbb{I}-\hat{\boldsymbol{k}}\hat{\boldsymbol{k}})\int_S \mathbf{f}_j(\mathbf{r}')e^{\mathrm{i}k\boldsymbol{r}'\cdot\hat{\mathbf{k}}}d\boldsymbol{r}'P_p(\hat{\mathbf{k}}\cdot\hat{\mathbf{r}})d\hat{\mathbf{k}}. \tag{24}$$

It is seen that we have reconstructed the electric field for all points with $r > d$ based on the far field. Unfortunately, the current situation is not yet satisfactory. Since $\boldsymbol{r}'$ and $\hat{\mathbf{r}}$ are present in the same integral, we still end up needing to calculate the interactions separately for all pairs of basis functions, and we know from before that this results in a system matrix that does not fit into the computer memory. Fortunately, this problem is easily solved. We apply the following decomposition

$$\boldsymbol{r} = \boldsymbol{D} + \boldsymbol{r} - \boldsymbol{D}, \tag{25}$$

where $\boldsymbol{D}$ is some vector. Instead of computing $[\mathbf{E}(\mathbf{f}_j)](\boldsymbol{r})$ for many values of $\boldsymbol{r}$, we can also compute $[\mathbf{E}(\tilde{\mathbf{f}}_j)](\boldsymbol{D})$ for a fixed $\boldsymbol{D}$, but with displaced source currents

$$\tilde{\mathbf{f}}_j(\boldsymbol{r}' + (\boldsymbol{D}-\boldsymbol{r})) = \mathbf{f}_j(\boldsymbol{r}'). \tag{26}$$

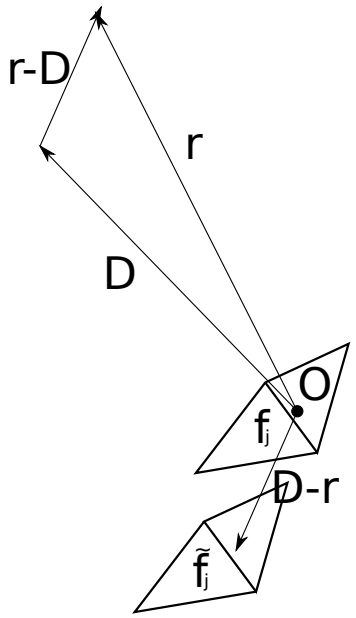

Fig. 3 original and displaced current distribution

The original and displaced current distribution are illustrated in Figure 3. The far field of this displaced source current is

$$\mathbf{E}(r\hat{\mathbf{r}}) = (\mathbb{I} - \hat{\boldsymbol{r}}\hat{\boldsymbol{r}})\frac{-\mathrm{i}ke^{-\mathrm{i}kr}}{4\pi r}\int_{\tilde{S}} \tilde{\mathbf{f}}_j(\boldsymbol{r}')e^{\mathrm{i}k\boldsymbol{r}'\cdot\hat{\mathbf{r}}}d\boldsymbol{r}', \tag{27}$$

with $\tilde{S}$ the displaced scatterer. We apply a change of variables $\boldsymbol{r}' \rightarrow \boldsymbol{r}' + \boldsymbol{r} - \boldsymbol{D}$ and find that the far field is given by

$$\mathbf{E}(r\hat{\mathbf{r}}) = (\mathbb{I} - \hat{\boldsymbol{r}}\hat{\boldsymbol{r}})\frac{-\mathrm{i}ke^{-\mathrm{i}kr}}{4\pi r}\int_{S} \mathbf{f}_j(\boldsymbol{r}')e^{\mathrm{i}k(\boldsymbol{r}'-(\boldsymbol{r}-\boldsymbol{D}))\cdot\hat{\mathbf{r}}}d\mathbf{r}'. \tag{28}$$

We can take out the new exponential factor and compute the electric field using (24), where, as mentioned, we substitute $r\hat{\mathbf{r}} = D\hat{\mathbf{D}}$ and the displaced source current to calculate the electric field at $r\hat{\mathbf{r}}$ due to the original source current

$$\mathbf{E}(r\hat{\mathbf{r}}) = \sum_{p=0}^{\infty} h_p^{(2)}(kD)\frac{-k^2(2p+1)}{(4\pi)^2(\mathrm{i})^p}\int_{\hat{S}} e^{\mathrm{i}k(-(\boldsymbol{r}-\boldsymbol{D}))\cdot\hat{\mathbf{k}}}(\mathbb{I}-\hat{\boldsymbol{k}}\hat{\boldsymbol{k}})\int_S \mathbf{f}_j(\mathbf{r}')e^{\mathrm{i}k\boldsymbol{r}'\cdot\hat{\mathbf{k}}}d\boldsymbol{r}'P_p(\hat{\mathbf{k}}\cdot\hat{\mathbf{D}})d\hat{\mathbf{k}}. \tag{29}$$

An alternative viewpoint is, that if we want to compute the electric field at $\boldsymbol{r}$, we shift the origin of the coordinate system by $\boldsymbol{r} - \boldsymbol{D}$. In the new coordinate system we then evaluate the electric field at $\boldsymbol{D}$, but with a far field radiation pattern computed with respect to the new origin. The current expression is still not suitable for a numerical method, since we would need to evaluate

an infinite sum for every basis function that is related to a test function. Therefore we truncate the multipole expansion at $p = P$ and interchange the integration and summation to obtain

$$\mathbf{E}(r\hat{\mathbf{r}}) \approx \int_{\hat{S}} e^{\mathrm{i}k(-(\boldsymbol{r}-\boldsymbol{D}))\cdot\hat{\mathbf{k}}} \left(\sum_{p=0}^{P} h_p^{(2)}(kr) \frac{-k^2(2p+1)}{(4\pi)^2(\mathrm{i})^p} P_p(\hat{\mathbf{k}}\cdot\hat{\mathbf{D}}) \right) (\mathbb{I}-\hat{\boldsymbol{k}}\hat{\boldsymbol{k}}) \int_S \mathbf{f}_j(\mathbf{r}') e^{\mathrm{i}k\boldsymbol{r}'\cdot\hat{\mathbf{k}}} d\boldsymbol{r}' d\hat{\mathbf{k}}. \tag{30}$$

We now have an expression that is suitable for a numerical method, because $\boldsymbol{r}$ and $\boldsymbol{r}'$ appear in different integrals. This means that the interactions between basis functions can be computed in clusters of basis functions. Suppose that we have two clusters G_m and $G_{m'}$ and that we want to compute the interactions between the basis functions in $G_{m'}$ with the electric field due to the basis functions in G_m

$$\sum_{j\in G_m} \mathcal{L}_{ij} J_j = \int_S \mathbf{f}_i(\boldsymbol{r}) \cdot \frac{-4\pi}{\eta} [\mathbf{E}(\sum_{j\in G_m} J_j \mathbf{f}_j)](\boldsymbol{r}) d\boldsymbol{r}, \quad i \in G_{m'}, \tag{31}$$

with J_j the surface current expansion coefficients. We then compute these interactions in three steps:

far field radiation pattern due to the current source $\sum_{j\in G_m} J_j \mathbf{f}_j$

$$\int_S \sum_{j\in G_m} J_j \mathbf{f}_j(\mathbf{r}') e^{\mathrm{i}k\boldsymbol{r}'\cdot\hat{\mathbf{k}}} d\boldsymbol{r}'.$$

transfer to a location in the center of cluster G_m, given by position vector $\mathbf{D}$, by multiplication with the transfer function

$$\left(\sum_{p=0}^{P} h_p^{(2)}(kr) \frac{-k^2(2p+1)}{(4\pi)^2(\mathrm{i})^p} P_p(\hat{\mathbf{k}}\cdot\hat{\mathbf{D}}) \right).$$

receiving patterns which are given by

$$\int_S \mathbf{f}_i(\mathbf{r}') e^{-\mathrm{i}k\boldsymbol{r}'\cdot\hat{\mathbf{k}}} d\boldsymbol{r}'.$$

The term receiving pattern is from [8].

The product of the transfer function and the far field radiation pattern is called an incoming wave in the literature. This term is related to a somewhat different derivation of the fast multipole method using a multipole expansion of a different type. We will not discuss this subject, but details can be found in [12] and [8].

It is seen that we now compute the interactions in clusters, and not pairwise between the basis functions.

There are some caveats. The transfer function (the sum inside the k-space integral in (30)) is actually divergent if we let $p \to \infty$, since the interchange of the summation and the integral is not a mathematically valid operation. This can cause numerical problems in some situations, see Section 6.3.

We also need to carefully examine on what domain expression (30) is valid. We had earlier assumed that $\mathbf{f}_j$ is contained inside $B(\mathbf{0}, d)$. Suppose that we want to evaluate the electric field in a unit sphere $B(\mathbf{D}, d)$, centered in $\mathbf{D}$. This is what we are doing in the example with cluster $G_{m'}$ above. Then the displaced currents are contained inside $B(\mathbf{0}, 2d)$ and the expression for the electric field is valid for $D > 2d$. This condition must not be violated in the FMM.

We can give the following physical interpretation of the incoming waves. The incoming waves are the coefficients in an (approximate) plane wave expansion of the electric field in the sphere $B(\mathbf{D}, d)$ due the current source in the sphere $B(\mathbf{0}, d)$. Note that this does not explain the name incoming waves.

As mentioned, an essential feature of the FMM is that interactions between basis functions are computed in clusters. We previously described how to compute the interactions between basis functions in two clusters $\sum_{j \in G_m} \mathcal{L}_{ij} J_j$. We will now describe the FMM where interactions are computed between all the basis functions $\sum_{j=1}^{N} \mathcal{L}_{ij} J_j$. For this, a cubic lattice is superimposed on the mesh. The analogous 2D case where a square lattice is superimposed on the mesh is illustrated in Figure 4. Each basis function is assigned to the cube containing the mid-point of its edge. We use the term cluster to denote the set of basis functions in a nonempty cube. Define G_m, the set of basis functions in cluster m, and $\boldsymbol{c}_m$, the center of the cube corresponding to cluster m.

These sets and variables are illustrated in Figure 4. As mentioned earlier, the FMM is a method for accelerating matrix-vector products, and it avoids explicitly calculating the system matrix $\mathcal{L}_{ij}$. However, mathematically, we can still see the FMM as calculating matrix-vector products with $\mathcal{L}_{ij}^p$, an approximation to the system matrix. We use the term interaction to describe individual entries $\mathcal{L}_{ij}^p$, corresponding to basis functions i and j. Interactions of basis functions in the same cluster are computed by directly using (12), instead of a multipole expansion, because the expressions for $\mathbf{E}$ we found earlier are not valid there. For the same reason, we also introduce a buffer zone: interactions between basis functions in adjacent cluster are calculated directly and not with the fast multipole method. In order to describe this, we define the interaction list G_m^{adj} for cluster m, the set of cluster adjacent to m in the cubic lattice, combined with m itself. This is illustrated in Figure 5, where the electric field due to a current source in the dark grey cube is computed directly in the dark grey and the light grey cubes. In the white cubes with arrows pointing to the center, and the cubes that are not included in the figure, it is computed with the

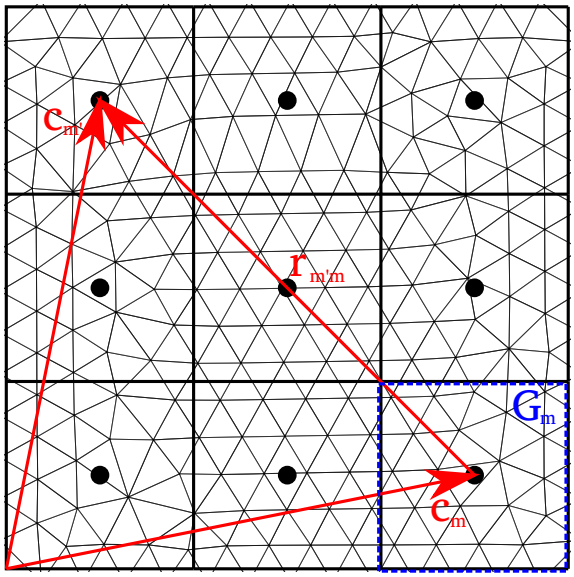

Fig. 4 interaction between two clusters in the FMM on a part of a plate mesh in the 2D case. The circles are cluster centers and the thick line segments are the edges of clusters. The thin line segments are edges corresponding to basis functions. The dashed blue line segments illustrate what basis functions are contained in cluster G_m.

FMM.

With these preliminaries out of the way, we can describe the FMM approximation to the matrix-vector products

$$
\begin{aligned}
J_i^{\text{output}} \;=\; & \sum_{j=1}^{N} \mathcal{L}_{ij} J_j^{\text{input}} \approx \mathrm{i}k \int_{\hat{S}} \underbrace{\left(\int_S \boldsymbol{f}_i e^{-\mathrm{i}k\hat{\boldsymbol{k}}\cdot(\boldsymbol{r}'-\boldsymbol{c}_{m'})} d\boldsymbol{r}' \right)}_{\text{receiving pattern}} \cdot \\
& \sum_{m \notin G_{m'}^{\text{adj}}} \underbrace{\alpha(k\hat{\boldsymbol{k}}, \boldsymbol{r}_{m'm})}_{\text{transfer}} \sum_{j \in G_m} \underbrace{(\mathbb{I} - \hat{\boldsymbol{k}}\hat{\boldsymbol{k}}) \left(\int_S \boldsymbol{f}_j e^{\mathrm{i}k\hat{\boldsymbol{k}}\cdot(\boldsymbol{r}-\boldsymbol{c}_m)} d\boldsymbol{r} \right)}_{\text{far field radiation pattern}} J_j^{\text{input}} d\hat{\boldsymbol{k}} \\
+ & \sum_{m \in G_{m'}^{\text{adj}}} \sum_{j \in G_m} \mathcal{L}_{ij} J_j^{\text{input}},
\end{aligned}
$$

with m' the cluster containing basis function i, J_i^{output} the i-th component of the output vector in the Krylov iteration, corresponding to basis function i, J_j^{input} the j-th component of the input vector at iteration r, corresponding to basis function j, and

$$
\begin{aligned}
\alpha(k\hat{\boldsymbol{k}}, \boldsymbol{r}_{m'm}) \;&:=\; \frac{k}{4\pi} \sum_{p=0}^{P} (-\mathrm{i})^{p+1} (2p+1) h_p^{(2)}(k|\boldsymbol{r}_{m'm}|) P_p(\hat{\boldsymbol{k}} \cdot \hat{\boldsymbol{r}}_{m'm}), \\
\boldsymbol{r}_{m'm} \;&:=\; \boldsymbol{c}_{m'} - \boldsymbol{c}_m,
\end{aligned}
$$

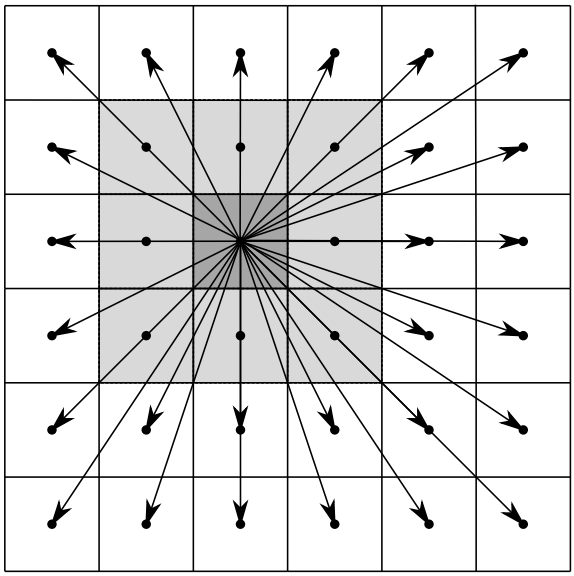

Fig. 5 transfer phase in the FMM and the MLFMA. This illustration is also used in the chapter about the MLFMA. Not all clusters are shown. In the FMM, the dark grey cluster also interacts with clusters that are not shown (that are farther away). In the MLFMA, the arrows indicate all the interaction for this cluster. Interactions between basis functions in clusters that are farther away are computed at a coarser level. The light grey indicates the buffer clusters.

with $h_p^{(2)}$ the spherical Hankel function of the second kind of order p, P the number of multipoles, and P_p the Legendre polynomial of degree p. The variables are illustrated in Figure 4. The far field radiation patterns, transfer function and receiving patterns are reused in all matrix-vector products and are precomputed in the initialization phase of the FMM. The k-space integral over $\hat{S}$ is evaluated numerically during the solution phase of the algorithm. More details on numerical quadrature of this integral is given in Section 6.3.

5.1 Derivation

The derivation in this section is gieven in [8]. Let the test and current basis functions $\boldsymbol{f}_i$ and $\boldsymbol{f}_j$ be contained in clusters with $G_{m'}$ and G_m with cluster centers $\boldsymbol{c}_{m'}$ and $\boldsymbol{c}_m$ respectively. Suppose that we are trying to find the electric field at $\boldsymbol{r}'$, in the domain of $\boldsymbol{f}_i$, due to a current at $\boldsymbol{r}$, in the domain of $\boldsymbol{f}_j$. We apply the following decomposition

$$\boldsymbol{r}' - \boldsymbol{r} = \boldsymbol{r}' - \boldsymbol{c}_{m'} + \boldsymbol{c}_{m'} - \boldsymbol{c}_m + \boldsymbol{c}_m - \boldsymbol{r} =: \boldsymbol{d}_{m'} + \boldsymbol{r}_{m'm} - \boldsymbol{d}_m. \tag{32}$$

Define

$$\begin{aligned} \boldsymbol{d} &:= \boldsymbol{d}_{m'} - \boldsymbol{d}_m, \\ \boldsymbol{D} &:= \boldsymbol{r}_{m'm}, \end{aligned}$$

and assume that $|\boldsymbol{d}| < |\boldsymbol{D}|$. The addition theorem (see [8]) states

$$\frac{e^{-\mathrm{i}k|\boldsymbol{D}+\boldsymbol{d}|}}{|\boldsymbol{D}+\boldsymbol{d}|} = -\mathrm{i}k \sum_{p=0}^{\infty} (-1)^p (2p+1) j_p(kd) h_p^{(2)}(kD) P_p(\hat{\boldsymbol{d}} \cdot \hat{\boldsymbol{D}}), \tag{33}$$

with $d = |\boldsymbol{d}|$, $D = |\boldsymbol{D}|$, and j_p the spherical Bessel function of the first kind of order p. See [3] for details about the spherical Bessel function of the second kind. The following plane-wave expansion can now be applied [8]

$$4\pi(-\mathrm{i})^p j_p(kd) P_p(\hat{\boldsymbol{d}} \cdot \hat{\boldsymbol{D}}) = \int_{\hat{S}} e^{-\mathrm{i}k\hat{\boldsymbol{k}}\cdot\boldsymbol{d}} P_p(\hat{\boldsymbol{k}} \cdot \hat{\boldsymbol{D}}) d\hat{\boldsymbol{k}}, \tag{34}$$

where $\hat{S}$ is the unit sphere. We now truncate the expansion (33), apply the plane-wave expansion, and interchange the integration and summation to obtain the following approximation to the Green's function

$$\frac{e^{-\mathrm{i}k|\boldsymbol{D}+\boldsymbol{d}|}}{|\boldsymbol{D}+\boldsymbol{d}|} \approx \int_{\hat{S}} e^{-\mathrm{i}k\hat{\boldsymbol{k}}\cdot\boldsymbol{d}} \alpha(k\hat{\boldsymbol{k}}, \boldsymbol{D}) d\hat{\boldsymbol{k}}, \tag{35}$$

with the transfer function

$$\alpha(k\hat{\boldsymbol{k}}, \boldsymbol{D}) := \frac{k}{4\pi} \sum_{p=0}^{P} (-i)^{p+1}(2p+1) h_p^{(2)}(kD) P_p(\hat{\boldsymbol{k}} \cdot \hat{\boldsymbol{D}}), \tag{36}$$

and P the number of multipole terms that we keep. Substituting the approximation to the Green's function into the weak formulation we find

$$\mathcal{L}_{ij} \approx \mathrm{i}k \int_{\hat{S}} \left(\int_S \boldsymbol{f}_i e^{-\mathrm{i}k\hat{\boldsymbol{k}}\cdot(\boldsymbol{r}'-\boldsymbol{c}_{m'})} d\boldsymbol{r}' \right) \alpha(k\hat{\boldsymbol{k}}, \boldsymbol{r}_{m'm})(\mathbb{I} - \hat{\boldsymbol{k}}\hat{\boldsymbol{k}}) \left(\int_S \boldsymbol{f}_j e^{\mathrm{i}k\hat{\boldsymbol{k}}\cdot(\boldsymbol{r}-\boldsymbol{c}_m)} d\boldsymbol{r} \right) d\hat{\boldsymbol{k}}. \tag{37}$$

In the literature this factorization is called a diagonalization of the transfer operator. This interpretation makes more sense in the context of the derivation of FMM in 2D in [8], where two separate multipole expansions are applied and a convolution theorem is applied.

6 Multilevel fast multipole algorithm

6.1 Description of the algorithm

In this chapter, the multilevel fast multipole algorithm (MLFMA) is described [8]. The MLFMA has $O(N \log N)$ CPU and memory costs. An essential feature of the MLFMA is that interactions between basis functions are calculated in clusters of varying sizes. Recall that in the FMM, we calculate interactions between basis functions in clusters of a fixed size. This means that interactions between a large number of clusters need to be calculated. The number of pairs of clusters can be reduced by using larger clusters. However, the FMM approximation to the interaction between two basis functions is only valid if they are in clusters separated by at least one other cluster, the buffer zone. Therefore interactions between basis functions in adjacent clusters or inside the same cluster are computed directly using (12). If the cluster size is increased, the number of interactions that need to be computed directly increases very quickly. The CPU costs of the additional direct interactions then outstrip the costs saved by computing fewer interactions between clusters. In the FMM, this actually leads to an optimization problem for the cube diameter.
In the MLFMA, interactions between basis functions are calculated in clusters that are as large as possible, given the condition that there still needs to fit a buffer inbetween. The distance over which the interactions between the clusters are computed, is then about two times the cube diameter. This is only possible in a multilevel structure, where interactions between distant basis functions are computed in large clusters. Interactions between basis functions that are closer to each others are computed in smaller clusters. For this, an octree is constructed. We use the word coarse to describe levels with large clusters. Levels with small clusters are described as fine. Define the levels $l = 0, \ldots, l_{\text{max}}$. At the coarsest level 0, a single cube contains the entire mesh. At

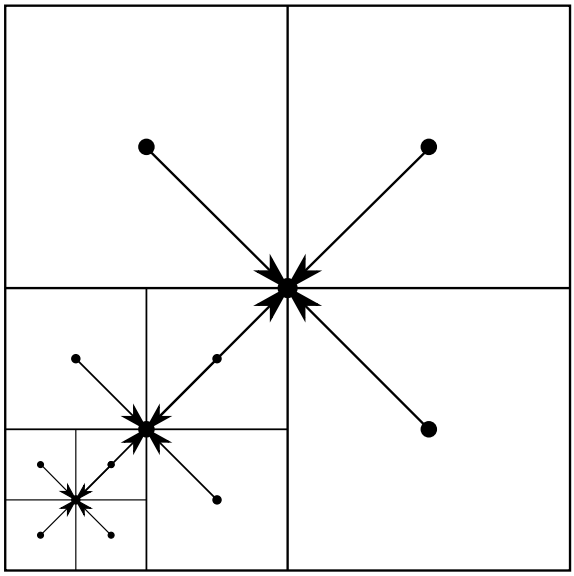

Fig. 6 aggregation in the MLFMA in 2D. The line segments indicate the edges of the boxes. In 3D these become cubes. The thick line segments indicate boxes at coarser levels and the thin line segments indicate boxes in finer levels. Not all the sub-boxes are shown. The circles indicate box centers. The arrows indicate the shifts in the aggregation. The circle in the center of the figure represents the box center of a single box at the finest level.

levels $l = 1, \ldots, l_{\text{max}}$, each cube is recursively subdivided into eight child cubes and only the nonempty ones are retained. At the finest level l_{max}, the nonempty cubes contain about 10 basis functions. Note that, inconsistently with this indexing, the coarser levels were described as higher levels in the introduction to this report. In Figure 6 the octree structure is illustrated in the 2D case. Define N_g^l, the number of clusters (nonempty cubes) at level l. The subscript g refers to group, another term that is used for the clusters in the literature. We use the following indices for the clusters at level l

$$m = 1, \ldots, N_g^l.$$

Also, define $\boldsymbol{c}_m^l$, the cube center corresponding to cluster m at level l. Define G_m^l for $l < l_{\text{max}}$, the set of child clusters of cluster m at level l. Furthermore, define $G_m^{l_{\text{max}}}$, the set of basis functions in cluster m at the finest level l_{max}. In the MLFMA, interactions between basis functions are calculated in clusters of the largest size such that they can still be separated by a buffer of a single other cluster. Specifically, a cluster m at level l interacts with $G_m^{\text{int},l}$, the set of nonempty child cubes of neighbours of the parent of m, that are not adjacent to m. This is illustrated in Figure 5 (see the chapter about the FMM), where the arrows indicate all the interactions computed at this level for basis functions in the dark grey cluster. Finally, define K_l, the number of

integration points used in the k-space integral at level l, $\hat{\boldsymbol{k}}_i^l$, the integration points, and ω_i^l, the quadrature weights. Recall that the integration points are also the directions used in the aggregation phase in the MLFMA.

A key step in the MLFMA is the use of interpolation. In the interaction between two clusters, we apply a transfer function to the far field radiation patterns. The motivation for interpolation is that the far field radiation pattern of a large cluster has a large spectral content. It therefore needs to be sampled at a large number directions. It is expensive to compute these k-space samples directly, since this involves integration over the surface of the scatterer. Now a large cluster is composed of a number of child clusters. These are smaller and the spectral content of their far field radiation patterns is also smaller. Their far field radiation patterns are therefore sampled at a smaller number of directions. We use the key step of interpolation to sample them at the larger number of directions of the parent cluster. The k-space samples of the parent cluster are then computed by summation over the interpolated k-space samples of the child clusters at each direction required for the parent cluster. This idea can also be applied to the child clusters and their child clusters and so on. This recursive process is called aggregation.

We did just neglect one additional step. The spectral content of the far field radiation pattern depends on the origin of the coordinate system with respect to which it is defined. The spectral content is smallest if the origin is at the center of a cluster. Therefore we ensure that the far field radiation patterns are always defined with respect to the cluster centers by applying shifts when aggregating from a finer level to a coarser level. These shifts are illustrated in Figure 6.

We will now describe the MLFMA in detail. It is divided into five stages.

summation over the k-space samples of the individual basis functions in each cluster at the finest level, at each direction

$$\boldsymbol{v}^{(o)}_{m,l_{\text{max}}}(\hat{\boldsymbol{k}}_i^{l_{\text{max}}}) := \sum_{j \in G_m^{l_{\text{max}}}} (\mathbb{I} - \hat{\boldsymbol{k}}_i^{l_{\text{max}}} \hat{\boldsymbol{k}}_i^{l_{\text{max}}}) \int_S \boldsymbol{f}_j e^{\mathrm{i}k\hat{\boldsymbol{k}}_i^{l_{\text{max}}} \cdot (\boldsymbol{r} - \boldsymbol{c}_m^{l_{\text{max}}})} d\boldsymbol{r} J_j^{\text{input}},$$

for $m = 1, \ldots, N_g^{l_{\text{max}}}$, $i = 1, \ldots, K_{l_{\text{max}}}$. The integral over S is precomputed for each value of $\hat{\boldsymbol{k}}_i^{l_{\text{max}}}$. The superscript (o) refers to outgoing waves.

aggregation where the far field radiation patterns at the levels $l = l_{\text{max}} - 1, \ldots, 2$ are recursively aggregated from fine to coarser levels

$$\boldsymbol{v}^{(o)}_{m,l}(\hat{\boldsymbol{k}}_j^l) := \sum_{m_c \in G_m^l} e^{\mathrm{i}k\hat{\boldsymbol{k}}_j^l \cdot (\boldsymbol{c}_{m_c}^{l+1} - \boldsymbol{c}_m^l)} \tilde{\boldsymbol{v}}^{(o)}_{m_c,l+1}(\hat{\boldsymbol{k}}_j^l),$$

for $m = 1, \ldots, N_g^l$, the directions at the coarser level $j = 1, \ldots, K_l$, with $\tilde{\boldsymbol{v}}^{(o)}_{m_c,l+1}(\hat{\boldsymbol{k}})$ the interpolated far field radiation pattern based on the k-space samples at the finer level $\boldsymbol{v}^{(o)}_{m_c,l+1}(\hat{\boldsymbol{k}}_i^{l+1})$, $i = 1, \ldots, K_{l+1}$. One can see that the interpolated far field radiation pattern is sampled at the directions of the coarser level. These samples are then the k-space

samples at the coarser level. This step is illustrated in Figure 6. We used the subscript c to indicate that an index refers to the child clusters.

transfer of the far field radiation patterns to the cube centers

$$\boldsymbol{v}^{(i),1}_{m^2,l}(\hat{\boldsymbol{k}}^l_i) := \sum_{m^1 \in G^{\text{int},l}_{m^2}} \omega^l_i \alpha(k\hat{\boldsymbol{k}}^l_i, \boldsymbol{c}^l_{m^2} - \boldsymbol{c}^l_{m^1}) \boldsymbol{v}^{(o)}_{m^1,l}(\hat{\boldsymbol{k}}^l_i),$$

for $m^2 = 1, \ldots, N^l_g, l = l_{\text{max}}, \ldots, 2$. The multipole expansion $\alpha(k\hat{\boldsymbol{k}}^l_i, \boldsymbol{c}^l_{m^2} - \boldsymbol{c}^l_{m^1})$ is precomputed during the initialization phase. We used the superscript $(i), 1$ to indicate that these are incomplete incoming waves. The incoming waves (coefficients of the approximate plane wave expansion of the electric field) computed in this step are only due to the source currents in clusters that interact at this level, instead of all the clusters. Note that the quadrature weights are applied at this step.

disaggregation where the incoming waves at the levels $l = 3, \ldots, l_{\text{max}}$[1] are disaggregated from the coarser to the finer level

$$\boldsymbol{v}^{(i),2}_{m,l}(\hat{\boldsymbol{k}}^l_j) := e^{-\mathrm{i}k\hat{\boldsymbol{k}}^l_j \cdot (\boldsymbol{c}^{l-1}_{m_p} - \boldsymbol{c}^l_m)} \tilde{\boldsymbol{v}}^{(i),2}_{m_p,l-1}(\hat{\boldsymbol{k}}^l_j) + \boldsymbol{v}^{(i),1}_{m,l}(\hat{\boldsymbol{k}}^l_j),$$

for $m_p = 1, \ldots, N^{l-1}_g$, for all $m \in G^{l-1}_{m_p}$, $j = 1, \ldots, K_l$, with $\tilde{\boldsymbol{v}}^{(i),2}_{m_p,l-1}(\hat{\boldsymbol{k}})$ the interpolated incoming waves based on the sample values $\boldsymbol{v}^{(i),2}_{m_p,l-1}(\hat{\boldsymbol{k}}^{l-1}_i)$ at the directions corresponding to the coarser level $i = 1, \ldots, K_{l-1}$. The interpolated incoming waves are sampled at the directions corresponding to the finer levels. Since there are fewer of these, we are undersampling the incoming waves. Note that in the disaggregation phase, the spectral content of the incoming waves is not expected to depend on the level. The reason for this is that the incoming waves represent the plane wave coefficients of the electric field (by approximation) due to current sources clusters that interact at this level or coarser levels. The electric field due to these has a larger spectral content than the electric field due to source currents in cluster that interact at finer levels or due to source currents in the buffer zone. The interpolations in this step are called anterpolations in the literature. They are the transpose of the interpolations in the aggregation. We use the subscript p to indicate the parent clusters.

testing where the new current coefficient vector is computed

$$J^{\text{output}}_j := \mathrm{i}k \sum_{i=1}^{K_{l_{\text{max}}}} (\mathbb{I} - \hat{\boldsymbol{k}}^{l_{\text{max}}}_i \hat{\boldsymbol{k}}^{l_{\text{max}}}_i) \int_S \boldsymbol{f}_j e^{-\mathrm{i}k\hat{\boldsymbol{k}}^{l_{\text{max}}}_i \cdot (\boldsymbol{r} - \boldsymbol{c}^{\text{max}}_m)} d\boldsymbol{r} \cdot \boldsymbol{v}^{(i),2}_{m,l_{\text{max}}}(\hat{\boldsymbol{k}}^{l_{\text{max}}}_i),$$

for $j = 1, \ldots, N$, with m the cluster that basis function j is located in. The integral over S is precomputed for each value of $\hat{\boldsymbol{k}}^{l_{\text{max}}}_i$.

[1] The incoming waves at the coarsest level $l = 2$ are identical to the transferred far field radiation patterns.

The term far field radiation patterns is used to describe different things in this report. The first possibility refers to the far field radiation patterns computed recursively above. It is also used to describe

$$\sum_{j\in G_m^{\mathrm{b},l}} \int_S \boldsymbol{f}_j e^{\mathrm{i}k\hat{\boldsymbol{k}}_i^l\cdot(\boldsymbol{r}-\boldsymbol{c}_m^l)} d\boldsymbol{r}, \tag{38}$$

with $G_m^{\mathrm{b},l}$ the set of basis functions in cluster m at level l. The far field radiation patterns $\boldsymbol{v}_{m,l}^{(o)}$ computed using the MLFMA are approximations of the above integral.

6.2 Lagrange interpolation in the MLFMA

Interpolation is an essential step in the MLFMA because it is too expensive to directly sample the far field radiation patterns directly at the coarser levels, corresponding to large clusters, where they have a large spectral content. Recall that we apply interpolation during the aggregation phase of the MLFMA, where we have the k-space samples of the far field radiation pattern at some level, and we use interpolation to find the k-space samples at the larger number of directions of the coarser level.

The standard interpolation method for the MLFMA in the literature is Lagrange interpolation. In this section we describe Lagrange interpolation. The directions used in the aggregation process match the integration points in the k-space integrals in the MLFMA. The continuous versions of the k-space integrals in the MLFMA are not given in this report, but they are similar to (32). The use of the integration points as directions in the aggregation is actually oversampling of the far field radiation patterns, but it is necessary in order to obtain a sufficiently small interpolation error.

We will now describe the integration points. Let L be some positive number. The integration points are the Gauss-Legendre quadrature points (θ_j, ϕ_i), $j = 1, \ldots, L$, $i = 1, \ldots, 2L$. In Gauss-Legendre quadrature, there are $2L$ equally-spaced integration points in the ϕ direction, and the points in the θ direction are the L zeros of P_L, the Legendre polynomial of degree L.

In our implementation, we use a $2p \times 2p$ stencil for the interpolation, where p is an interpolation parameter. In our implementation, we use $p = 3$, resulting in an interpolation error that is smaller than $\epsilon = 0.001$ in our tests. The formula for Lagrange interpolation in the scalar case is

$$\tilde{f}(\theta,\phi) = \sum_{i=s+1-p}^{s+p} \omega_i(\phi) \sum_{j=t+1-p}^{t+p} v_j(\theta) f(\theta_j,\phi_i), \tag{39}$$

with $\tilde{f}(\theta,\phi)$ the interpolated function and $f(\theta_j,\phi_i)$ the sample values at the interpolation points (θ_j,ϕ_i). We have that (t,s) depends on the target point (θ,ϕ). The interpolators are given by

$$\omega_i(\phi) = \prod_{k=s+1-p,k\neq i}^{s+p} \frac{\phi-\phi_k}{\phi_i-\phi_k}, \tag{40}$$

and

$$v_j(\theta) = \prod_{l=t+1-p, l\neq j}^{t+p} \frac{\theta - \theta_l}{\theta_j - \theta_l}. \tag{41}$$

We actually use a two-step process for the Lagrange interpolation, in order to reduce CPU times. In the first step we determine interpolations $\tilde{f}_1(\phi, \theta_i)$, separately for all values of θ_i corresponding to sample points at the previous level, and we evaluate the interpolations at all the $\phi = \phi_j$ corresponding to target points at the new level. In the second step we determine interpolations $\tilde{f}_2(\phi_j, \theta)$, separately for all values of ϕ_j corresponding to target points at the new level, and we evaluate the interpolations at the target points $\theta = \theta_l$ corresponding to the new level.

6.3 Parameters and error sources in the MLFMA

There are two important parameters in the MLFMA that we will discuss together with their associated errors in this chapter:

- The choice of directions $\hat{\mathbf{k}}_j^l$ and the integration error,
- The number of multipole terms P_l in the transfer function $\alpha(k\hat{\boldsymbol{k}}_i^l, \boldsymbol{c}_{m_l^2}^l - \boldsymbol{c}_{m_l^1}^l)$ and the truncation error.

We will also discuss the interpolation error.

6.3.1 Choice of directions

Recall that the directions $\hat{\mathbf{k}}_j^l$ at level l in the aggregation in the MLFMA match the integration points at that level in the k-space integral. The reasons for this are that accurate Lagrange interpolation requires oversampling of the far field patterns and that reconstruction of large number of k-space samples from a smaller number introduces a new CPU cost. It is awkward to write down this k-space for the MLFMA and we have not done so in this report. The integration points are determined by the requirement that the numerical integration k-space integral is accurate. In order to avoid a mess of notation we will consider the choice of integration points in the k-space integral in the FMM

$$\int_{\hat{S}} \underbrace{\left(\int_S \boldsymbol{f}_i e^{-\mathrm{i}k\hat{\boldsymbol{k}}\cdot(\boldsymbol{r}'-\boldsymbol{c}_{m'})} d\boldsymbol{r}' \right)}_{\text{receiving pattern}} \cdot \sum_{m\notin G_{m'}^{\text{adj}}} \underbrace{\alpha(k\hat{\boldsymbol{k}}, \boldsymbol{r}_{m'm})}_{\text{transfer}} \sum_{j\in G_m} \underbrace{(\mathbb{I} - \hat{\boldsymbol{k}}\hat{\boldsymbol{k}}) \left(\int_S \boldsymbol{f}_j e^{\mathrm{i}k\hat{\boldsymbol{k}}\cdot(\boldsymbol{r}-\boldsymbol{c}_m)} d\boldsymbol{r} \right)}_{\text{far field radiation pattern}} J_j^{\text{input}} d\hat{\boldsymbol{k}}. \tag{42}$$

The results can be immediately extended to the MLFMA. In this report we apply the Gauss-Legendre quadrature rule. Let L be some positive number. In Gauss-Legendre quadrature, there are $2L$ equally-spaced integration points in the ϕ direction, and the points in the θ direction are the L zeros of P_L, the Legendre polynomial of degree L. It can be seen that the total number of

integration points is $K = 2L^2$. The error due to numerical integration of the k-space integral is negligible if sufficient integration points are used [25], namely $L = P + 1$.[2] The key idea here is that, due to the orthogonality of the spherical harmonics used in the underlying analysis, only polynomial terms in the integrand in the k-space integral up to degree $2P$ have a nonzero contribution to the integral, and these can be numerically integrated exactly for $L = P + 1$. The integration error is then due to polynomial terms with degree $2P + 1$ and higher, that analytically integrate to zero but not numerically. In practice, the integration error is much smaller than the error due to the truncation of the multipole expansion and the interpolation error. The extension to the MLFMA is immediate. We then find that the number of directions is given by $K_l = 2(P_l + 1)^2$, with P_l the number of multipole terms.

6.3.2 Number of multipole terms

Finally, we will consider the number of multipole terms P_l in the transfer function $\alpha(k\hat{\boldsymbol{k}}_i^l, \boldsymbol{c}_{m_l^2}^l - \boldsymbol{c}_{m_l^1}^l)$. In the literature, the relative error in either (33) or (35) of the FMM due to the truncation of the multipole expansion is analyzed. This is also called the truncation error in the literature. The results can be immediately extended to the MLFMA. We make the following remarks on these analyses:

- The asymptotic analyses of the relative error in (33) in [8] and [32] are parameter-dependent. They rely on assumptions such as $\frac{D}{d} \to \infty$, $kd \to \infty$ and other approximations, that need to be validated empirically for our problem parameters. We have found in fact, that the analyses in [8] and [32] are invalid for our parameters.
- In computer implementations, the relative error in (35) is not controllable to arbitrary precision by using a high enough P, because the transfer function (36) is a divergent series, and we cannot accurately subtract very large numbers in finite precision arithmetic [20]. This is called the low-frequency breakdown. This divergence is a result of the fact that the interchange of the series and integral in the derivation of (35) is not mathematically valid if the series is not truncated. In levels where the cube diameter d_l is small compared to the wavelength, this severely constrains the obtainable accuracy. In fact, the relative error in (35) is not controllable to accuracy $\epsilon = 0.001$ for certain $\mathbf{d}$ and $\mathbf{D}$ in the levels with $d_l < \lambda$.

In [8] the so-called excess bandwidth formula is derived using asymptotic analysis. This is an estimate of the number of multipole terms required to approximate the Green's function (33) with d_0 digits of accuracy

$$P_l = kd_l + 1.8d_0^{2/3}(kd_l)^{1/3}, \tag{43}$$

[2] The quadrature rule can be made slightly more efficient by using $2P + 1$ integration points in the ϕ direction and $P + 1$ integration points in the θ direction [8].

l	P_l	K_l
11	6	128
10	8	200
9	12	392
8	19	882
7	31	2178
6	54	6272
5	97	19602
4	182	67712
3	348	245000
2	676	919368

Table 1 Characteristics of the MLFMA for a realistic aircraft at 10GHz

with d_l the cube diameter at level l. In this report, we use $d_0 = 3$, which is satisfactory for radar-cross section computations. Our tests indicate that this formula underestimates the required number of multipoles for $d_l < \lambda$. However, integral tests of the MLFMA performed at the National Aerospace Laboratory indicate that this does not result in an overall relative error that is larger than $\epsilon = 0.001$. In Table 1 the number of multipoles and directions at the different levels is given for a realistic simulation. The cube diameter at the finest level is $d_c = 0.25\lambda$. The diameter d_l of the cubes at level l is given by

$$d_l = 2^l d_c.$$

6.3.3 Interpolation error

We define the interpolation error for a cluster m_l at level l as

$$\epsilon^l = \max_{\hat{\boldsymbol{k}}_i^l} \frac{|\boldsymbol{v}_{m_l,l}^{(o)}(\hat{\boldsymbol{k}}_i^l) - \sum_{j \in G_{m_l}^{\mathrm{b},l}} \int_S \boldsymbol{f}_j e^{\mathrm{i}k\hat{\boldsymbol{k}}_i^l \cdot (\boldsymbol{r} - \boldsymbol{c}_{m_l}^l)} d\boldsymbol{r}|}{|\sum_{j \in G_{m_l}^{\mathrm{b}}} \int_S \boldsymbol{f}_j e^{\mathrm{i}k\hat{\boldsymbol{k}}_i^l \cdot (\boldsymbol{r} - \boldsymbol{c}_{m_l}^l)} d\boldsymbol{r}|},$$

with $G_{m_l}^{\mathrm{b},l}$ the set of basis functions in cluster m_l at level l. The interpolation error is of the same order as the truncation error if K_l directions are used in the aggregation.

7 Spherical harmonics expansion of the far field radiation patterns of the individual basis functions at the finest level

In this chapter the scheme from [13] is described, which reduces the sample rate of the far field radiation patterns of the individual basis functions at the finest level by a factor of eight. The motivation is to reduce the memory requirements of the MLFMA. These are dominated by the costs of storing the far field radiation patterns of the individual basis functions at the finest level. These need to be stored for all the individual basis functions, whereas the interpolation matrices at the higher levels can be applied to many different clusters. Recall that in the standard MLFMA we store the far field radiation pattern at the finest level in k-space samples $\boldsymbol{v}^{(o)}_{j,m_{l_{\max}+1}}$, at the directions $\hat{\boldsymbol{k}}_i^{l_{\max}}$. This is called the k-space representation in [13]. It is possible to use an interpolation strategy to reproduce the the far field radiation pattern based on a smaller number of underlying functions. The interpolants are given by the spherical harmonics

$$Y_p^q(\theta,\phi) := (-1)^q \left[\frac{(p-q)!}{(p+q)!}\frac{2p+1}{4\pi}\right]^{1/2} P_p^q(\cos(\theta))e^{\mathrm{i}q\phi}, \tag{44}$$

with p the degree, q the order, and P_p^q the associated Legendre polynomial of degree p and order q [3]. The spherical harmonics are the analog on the unit sphere of the Fourier basis functions in 1D. The spherical harmonics are an efficient representation of functions where the spectral content is concentrated in the lower frequencies, as is the case for the far field radiation patterns. A key property of the spherical harmonics is that they are an orthonormal basis for functions on the unit sphere in the L^2-inner product. The spherical harmonics expansion of a scalar function f on the surface of the unit sphere is given by

$$f(\hat{\boldsymbol{k}}) = \sum_{p=0}^{S}\sum_{q=-p}^{p} f_{pq}Y_p^q(\hat{\boldsymbol{k}}), \tag{45}$$

with S the degree of the spherical harmonics expansion and spherical harmonics coefficients

$$f_{pq} = \int_{\hat{S}} f(\hat{\boldsymbol{k}})Y_p^{q*}(\hat{\boldsymbol{k}})d\hat{\boldsymbol{k}}, \tag{46}$$

with $(\cdot)^*$ the complex conjugate. The central idea in this chapter is to store the spherical harmonics coefficients f_{pq} of the far field radiation patterns of the individual basis functions at the finest level rather than the k-space values, and to reconstruct the k-space values (which are multiplied by the transfer function in the MLFMA) for all the clusters at the finest level during the iterations.

It can be seen that this results in considerable memory savings. The spherical harmonics coefficients of the far field radiation patterns decay rapidly for $p > P_{l_{\max}}/2$ [25]. In other words, the

far field radiation patterns have a limited spectral content. Due to this rapid decay the spherical harmonics expansion can be truncated at $S = P_{l_{\max}}/2$. It is straightforward to show that a spherical harmonics expansion of degree S contains $(S+1)^2$ terms. This means that the sample rate is $(P_{l_{\max}}/2+1)^2$ if the spherical harmonics expansion is used. On the other hand, in the standard MLFMA the far field radiation patterns for the individual basis functions are stored at $2P_{l_{\max}}^2$ directions. This suggests that the interpolation strategy reduces the required amount of memory by a factor of about eight. On the other hand, if the spherical harmonics expansion is used to store the far field radiation patterns, all three Cartesian components need to be stored due to the Gibbs phenomenom, whereas for the k-space representation only the tangential components need to be stored [13]. The Gibbs phenomenom is a result of the fact that the unit vectors in the spherical coordinate system are discontinuous at the poles. That said, the spectral content of the Cartesian components of the far field radiation patterns is smaller than that of the tangential components. Therefore it is expected that the reduction in memory is between a factor of five and a factor of eight [13].

As a motivation, we will discuss why so many directions are used in the ordinary MLFMA. Recall that the fast multipole method is based on the k-space integrals

$$\mathrm{i}k \int_{\hat{S}} \left(\int_S \mathbf{f}_i e^{-\mathrm{i}k\hat{\mathbf{k}}\cdot(\mathbf{r}'-\mathbf{c}_{m'})} d\mathbf{r}' \right) \alpha(k\hat{\mathbf{k}}, \mathbf{r}_{m'm}) \left((\mathbb{I} - \hat{\boldsymbol{k}}\hat{\boldsymbol{k}}) \int_S \mathbf{f}_j e^{\mathrm{i}k\hat{\mathbf{k}}\cdot(\mathbf{r}-\mathbf{c}_m)} d\mathbf{r} \right) d\hat{\mathbf{k}}. \tag{47}$$

The far field radiation patterns $\left((\mathbb{I} - \hat{\boldsymbol{k}}\hat{\boldsymbol{k}}) \int_S \mathbf{f}_j e^{\mathrm{i}k\hat{\mathbf{k}}\cdot(\mathbf{r}-\mathbf{c}_m)} d\mathbf{r} \right)$ decay rapidly for $p > P_{l_{\max}}/2$ if they are represented by spherical harmonics. The receiving patterns $\left(\int_S \mathbf{f}_i e^{-\mathrm{i}k\hat{\mathbf{k}}\cdot(\mathbf{r}'-\mathbf{c}_{m'})} d\mathbf{r}' \right)$ also decay rapidly for $p > P_{l_{\max}}/2$ if they are represented by spherical harmonics. The transfer functions $\alpha(k\hat{\mathbf{k}}, \mathbf{r}_{m'm})$ decay rapidly for $p > P_{l_{\max}}$. The truncation number is two times as large in the transfer function as in the far field radiation pattern, due to the fact that $|\mathbf{r}_{m'm}| > 2d := 2\max_{\mathbf{r}}(\mathbf{r} - \mathbf{c}_m)$. Here d is one-half the cube diameter, and $\mathbf{r}_{m'm}$ is the distance over which the interactions between the clusters are computed. In the MLFMA we have $|\mathbf{r}_{m'm}| \approx 2d := 2\max_{\mathbf{r}}(\mathbf{r} - \mathbf{c}_m)$. It can now be seen that the quadrature rule must be chosen so that polynomials of degree $2P_{l_{\max}}$ are integrated exactly. The required number of integration points is then $K_{l_{\max}} = 2P_{l_{\max}}^2$, for integration of polynomials on the surface of the unit sphere, see Section 6.3.1. This results in a considerable oversampling of the far field radiation patterns, which decay rapidly for $p > P_{l_{\max}}/2$. Note that $P_{l_{\max}}$ depends on how small we want to make the truncation error, see Section 6.3.2. In this report we require that the truncation error is smaller than $\epsilon < 0.001$. In principle we could also store the far field radiation patterns using a smaller number of k-space samples, instead of the spherical harmonics. We will see that this results in a scheme that is less good than storing spherical harmonics. The spherical harmonics coefficients can be determined

using the formula

$$\int_{\hat{S}} \left((\mathbb{I} - \hat{\boldsymbol{k}}\hat{\boldsymbol{k}}) \int_S \mathbf{f}_j e^{\mathrm{i}k\hat{\mathbf{k}}\cdot(\mathbf{r}-\mathbf{c}_m)} d\mathbf{r} \right) Y_p^q(\hat{\mathbf{k}})^* d\hat{\mathbf{k}}. \tag{48}$$

We only need to be able to determine the spherical harmonics coefficients up to degree $P_{l_{\max}}/2$. If the far field radiation patterns are stored in k-space samples, then the spherical harmonics coefficients are not actually reconstructed in the algorithm, but the spherical harmonics up to degree $P_{l_{\max}}/2$ need to be implicit in the stored far field radiation pattern, for the validity of the truncation error analysis in the literature. We then need to be able to integrate exactly a polynomial of degree $P_{l_{\max}}$. For this, we need $P_{l_{\max}}^2/2$ directions. This is already a considerable reduction of the sample rate. However, the sample rate is only reduced by a factor of four, instead of a factor of eight if the spherical harmonics are used. This also means that the reconstruction of the k-space samples at the integration points of (47) will be more expensive than if spherical harmonics coefficients are stored.

7.1 Detailed description

The summation step of the MLFMA (see Section 6) is modified in the following way:

summation over the spherical harmonics coefficients of the far field radiation pattern of the individual basis functions in each cluster at the finest level

$$\mathbf{f}_{rs}^m := \sum_{j \in G_m^{l_{\max}}} \int_{\hat{S}} \boldsymbol{v}_{j,l_{\max}+1}^{(o)}(\hat{\boldsymbol{k}}) Y_r^{s*}(\hat{\boldsymbol{k}}) d\hat{\boldsymbol{k}} J_j^{\text{input}},$$

for $m = 1, \ldots, N_g^{l_{\max}}$, $r = 0, \ldots, S$, $s = -r, \ldots, r$, and with $\boldsymbol{v}_{j,l_{\max}+1}^{(o)}$ the far field radiation pattern for the individual basis functions

$$\boldsymbol{v}_{j,l_{\max}+1}^{(o)}(\hat{\boldsymbol{k}}) := \int_S \boldsymbol{f}_j e^{\mathrm{i}k\hat{\boldsymbol{k}}\cdot(\boldsymbol{r}-\boldsymbol{c}_m^{l_{\max}})} d\boldsymbol{r}.$$

The k-space integral is precomputed in the initialization phase of the algorithm.

reconstruction of the k-space samples at the finest level $l_{\max}$

$$\boldsymbol{v}_{m,l_{\max}}^{(o)}(\hat{\boldsymbol{k}}_i^{l_{\max}}) := \sum_{r=0}^{S} \sum_{s=-r}^{r} Y_r^s(\hat{\boldsymbol{k}}_i^{l_{\max}}) \mathbf{f}_{rs}^m,$$

for $m = 1, \ldots, N_g^{l_{\max}}$. If this expansion is implemented naively, then the computational complexity is $O(S^4)$. Using a trivial modification this can be accelerated to $O(S^3)$, and using the fast spherical harmonic transform it can be accelerated to $O(S^2 \log S)$ [30]. In the actual algorithm we include quadrature weights $\sqrt{\omega_i^{\hat{S}}}$ (from Gauss-Legendre quadrature of the k-space integrals at the finest level in MLFMA) so that the steps taken after

the application of the transfer function are the transpose of the steps taken before the application of the transfer function. This does not have a physical interpretation. The trivial modification is described in Section 8.6.

The testing step (see Section 6) is also modified:

spherical harmonics expansion of the incoming waves at the finest level l_{max}

$$\mathbf{g}_{rs}^{m} := \sum_{i=1}^{K_{l_{\text{max}}}} \omega_i^{\hat{S}} \boldsymbol{v}_{m,l_{\text{max}}}^{(i),2}(\hat{\boldsymbol{k}}_i^{l_{\text{max}}}) Y_r^{s*}(\hat{\boldsymbol{k}}_i^{l_{\text{max}}}),$$

for $m = 1, \ldots, N_g^{l_{\text{max}}}$, $r = 0, \ldots, S$, $s = -r, \ldots, r$. Note that we use sufficient integration points in this numerical integration, because $K_{l_{\text{max}}}$ is sufficient to integrate polynomials of degree $2P_{l_{\text{max}}}$ and the incoming waves $\boldsymbol{v}_{m,l_{\text{max}}}^{(i),2}$ decay rapidly for $p > P_{l_{\text{max}}}$. In the algorithm we actually use quadrature weights $\sqrt{\omega_i^{\hat{S}}}$ so that the steps taken after the application of the transfer function are the transpose of the steps taken before the application of the transfer function. This does not have a physical interpretation.

testing where the surface current expansion coefficient vector in the new Krylov iteration is computed

$$J_j^{\text{output}} := \mathrm{i}k \sum_{r=0}^{S} \sum_{s=-r}^{r} (\mathbf{f}_{rs}^{j,m})^* \cdot \mathbf{g}_{rs}^{m},$$

for $j = 1, \ldots, N$, with m the cluster that basis function j is located in, and with $\mathbf{f}_{rs}^{j,m}$ the spherical harmonics coefficients of far field radiation patterns of the individual basis functions

$$\mathbf{f}_{rs}^{j,m} := \int_{\hat{S}} \boldsymbol{v}_{j,l_{\text{max}}+1}^{(o)}(\hat{\boldsymbol{k}}) Y_r^{s*}(\hat{\boldsymbol{k}}) d\hat{\boldsymbol{k}},$$

which are the conjugate transpose of the receiving patterns. The $\mathbf{f}_{rs}^{j,m}$ are precomputed. In the derivation of the testing step the orthogonality of the spherical harmonics is used.

We use spherical harmonics expansions of the same degree (up to $p = P_{l_{\text{max}}}/2$) to represent both the far field radiation patterns and the incoming waves, despite the higher spectral content of the incoming waves. We are here following the argument in [13] that the spherical harmonics coefficients of the incoming waves, which decay rapidly for $p > P_{l_{\text{max}}}$, are multiplied by the spherical harmonics coefficients of the receiving pattern in the final testing step, which decay rapidly for $p > P_{l_{\text{max}}}/2$.

7.2 Use of symmetry to reduce the sample rate

In [13] it is mentioned that the symmetry of the far fields radiation patterns

$$\boldsymbol{v}_{m,l_{\text{max}}}^{(o)}(\hat{\boldsymbol{k}}) = \boldsymbol{v}_{m,l_{\text{max}}}^{(o)*}(-\hat{\boldsymbol{k}}), \tag{49}$$

has been used to reduce the storage costs. In [13] the complex spherical harmonics, were used to store the far field radiation patterns. The complex spherical harmonics are the spherical harmonics that have been used so far in the report. The effect of the symmetry on the coefficients with respect to the spherical harmonics is

$$\operatorname{Re} \mathbf{f}_{rs}^{j,m} = (-1)^{r+s} \operatorname{Re} \mathbf{f}_{r,-s}^{j,m*}, \tag{50}$$

$$\operatorname{Im} \mathbf{f}_{rs}^{j,m} = -(-1)^{r+s} \operatorname{Im} \mathbf{f}_{r,-s}^{j,m*}. \tag{51}$$

The symmetry can be used to realize a reduction in memory requirements by reconstructing the spherical harmonics coefficients for negative order based on the spherical harmonics coefficients for positive order during the solution phase of the algorithm. The spherical harmonics coefficients for negative order then do not need to be explicitly stored in the computer's memory, resulting in memory savings. The number of spherical harmonics coefficients that need to be stored is then decreased by a factor of about two. The same trick can of course also be applied to the ordinary MLFMA by storing the k-space samples only on one-half of the unit sphere.

8 Spherical harmonics based aggregation

8.1 Applying shifts to the spherical harmonics expansions

The spherical harmonics representation of the far field radiation pattern can also be used at coarser levels in the aggregation phase of the MLFMA, instead of just the summation step at the finest level (see Section 7.1). Recall that shifts were necessary in the aggregation phase of the MLFMA, because the spectral content of a far field radiation pattern is smallest if it is defined with respect to the coordinate system with the origin in the center of the cluster. The clusters become larger and larger as we aggregate to the coarser levels, and the centers shift, necessitating shifts of the origin with respect to which the the far field radiation pattern is defined. Recall that in the k-space representation a shift can be applied to the far field radiation pattern by multiplying the k-space samples by $e^{\mathrm{i}k\mathbf{k}_i\cdot\mathbf{d}} f(\hat{\mathbf{k}}_i)$, with $\mathbf{d}$ the distance of the shift. The shifts are illustrated for a few levels in Figure 6.

The central idea in this section is that we directly apply the shifts to the spherical harmonics expansion of the far field radiation patterns, and not to the k-space samples. The motivation for this, is that it results in a matrix that is small (due to the reduced sample rate) and dense, rather than large and sparse for Lagrange interpolation. If the spherical harmonics are used to represent the far field radiation patterns, then during the aggregation phase we compute recursively the

spherical harmonics expansions at $l = l_{\max} - 1, \ldots, 2$

$$\mathbf{f}_{pq}^{m,l} := \sum_{m_c \in G_m^l} \sum_{r=0}^{S_{l+1}} \sum_{s=-r}^{r} \int_{\hat{S}} Y_r^s(\hat{\boldsymbol{k}}) e^{\mathrm{i}k\hat{\boldsymbol{k}}\cdot(\boldsymbol{c}_{m_c}^{l+1} - \boldsymbol{c}_m^l)} Y_p^{q*}(\hat{\boldsymbol{k}}) d\hat{\boldsymbol{k}} \mathbf{f}_{rs}^{m_c,l+1}, \tag{52}$$

for $m = 1, \ldots, N_g^l$, $p = 0, \ldots, S_l$, $q = -p, \ldots, p$. We used the subscript in m_c to denote the child clusters The k-space integral is precomputed during the initialization phase, and it needs to be computed for at most eight distinct values of $\boldsymbol{c}_{m_c}^{l+1} - \boldsymbol{c}_m^l$ (consider the octree structure). Due to the truncation of the expansion over r the spherical harmonics coefficients $\mathbf{f}_{pq}^{m,l}$ here are only approximately equal to the exact spherical harmonics coefficients of the far field radiation pattern. If the spherical harmonics shift is implemented naively, then its asymptotic complexity is $O(S^4)$. It will be seen that this can be reduced to $O(S^3)$ using a straightforward factorization with rotations and a shift along the z-axis. In the aggregation phase of the MLFMA, the spherical harmonics representation of the far field radiation pattern at the finer levels can be combined with the k-space representation (and Lagrange interpolation) at the coarser levels, where the number of clusters is small and the number of multipoles is large. During the disaggregation phase we compute the incoming waves at the levels $l = 2, \ldots, l_{\max}$

$$\mathbf{g}_{pq}^{2,m,l} := \sum_{r=0}^{S_{l-1}} \sum_{s=-r}^{r} \int_{\hat{S}} Y_r^s(\hat{\boldsymbol{k}}) e^{\mathrm{i}k\hat{\boldsymbol{k}}\cdot(\boldsymbol{c}_{m_p}^{l-1} - \boldsymbol{c}_m^l)} Y_p^{q*}(\hat{\boldsymbol{k}}) d\hat{\boldsymbol{k}} \mathbf{g}_{rs}^{2,m_p,l-1} + \mathbf{g}_{pq}^{1,m,l}, \tag{53}$$

for $m_p = 1, \ldots, N_g^{l-1}$, $m \in G_{m_p}^{l-1}$, $p = 0, \ldots, S_l$, $q = -p, \ldots p$. We used the subscript in m_p to denote the parent clusters. One can see that we use spherical harmonics expansions of the same degree to represent both the far field radiation patterns and the incoming waves. In this we are extending the convention in [13] to the coarser levels.

8.2 Derivation

In this section we will show that the spherical harmonics coefficients computed using (52) are approximations to the spherical harmonics coefficients of the exact far field radiation patterns. Suppose that we are trying to calculate the exact spherical harmonics coefficients of the exact far field radiation patterns at level l, for cluster m. We find

$$\mathbf{f}_{pq}^{m,l} := \int_{\hat{S}} \sum_{j \in G_m^{\mathrm{b},l}} \int_S \boldsymbol{f}_j e^{\mathrm{i}k\hat{\boldsymbol{k}}\cdot(\boldsymbol{r} - \boldsymbol{c}_m^l)} d\boldsymbol{r} Y_p^{q*}(\hat{\boldsymbol{k}}) d\hat{\boldsymbol{k}}. \tag{54}$$

The exact far field radiation pattern at level l of cluster m is the sum of the exact far field radiation patterns of the child clusters, but with shifts applied to the origins

$$\int_{\hat{S}} \sum_{m_c \in G_m^l} e^{\mathrm{i}k\hat{\boldsymbol{k}}\cdot(\boldsymbol{c}_{m_c}^{l+1} - \boldsymbol{c}_m^l)} \sum_{j \in G_{m_c}^{b,l+1}} e^{\mathrm{i}k\hat{\boldsymbol{k}}\cdot(\boldsymbol{r} - \boldsymbol{c}_{m_c}^{l+1})} d\boldsymbol{r} Y_p^{q*}(\hat{\boldsymbol{k}}) d\hat{\boldsymbol{k}}. \tag{55}$$

We can apply a spherical harmonics expansion to the exact far field radiation patterns of the child clusters

$$\int_{\hat{S}} \sum_{m_c \in G_m^l} e^{\mathrm{i}k\hat{\boldsymbol{k}}\cdot(\boldsymbol{c}_{m_c}^{l+1}-\boldsymbol{c}_m^l)} \sum_{r=0}^{\infty}\sum_{s=-r}^{r} Y_r^s(\hat{\boldsymbol{k}})\boldsymbol{f}_{rs}^{m_c,l+1} Y_p^{q*}(\hat{\boldsymbol{k}})d\hat{\boldsymbol{k}}. \tag{56}$$

We truncate this spherical harmonics expansion

$$\int_{\hat{S}} \sum_{m_c \in G_m^l} e^{\mathrm{i}k\hat{\boldsymbol{k}}\cdot(\boldsymbol{c}_{m_c}^{l+1}-\boldsymbol{c}_m^l)} \sum_{r=0}^{S_{l+1}}\sum_{s=-r}^{r} Y_r^s(\hat{\boldsymbol{k}})\boldsymbol{f}_{rs}^{m_c,l+1} Y_p^{q*}(\hat{\boldsymbol{k}})d\hat{\boldsymbol{k}}. \tag{57}$$

Rearranging terms we find the expression for applying shifts to the spherical harmonics expansions (52)

$$\sum_{m_c \in G_{m^l}} \sum_{r=0}^{S_{l+1}}\sum_{s=-r}^{r} \int_{\hat{S}} Y_r^s(\hat{\boldsymbol{k}}) e^{\mathrm{i}k\hat{\boldsymbol{k}}\cdot(\boldsymbol{c}_{m_c}^{l+1}-\boldsymbol{c}_m^l)} Y_p^{q*}(\hat{\boldsymbol{k}})d\hat{\boldsymbol{k}}\mathbf{f}_{rs}^{m_c,l+1}. \tag{58}$$

In this context the $\mathbf{f}_{rs}^{m_c,l+1}$ are exact spherical harmonics, and in the aggregation phase of the MLFMA they are approximate above the next-to-finest level.

8.3 Shifts along the z-axis

In this section it is shown that spherical harmonics with different orders do not interact in shift along the z-axis. Suppose that $\mathbf{D} = D\mathbf{e}_z$. The interactions are given by

$$\int_{\hat{S}} Y_r^s(\hat{\mathbf{k}}) e^{\mathrm{i}k\hat{\mathbf{k}}\cdot(D\mathbf{e}_z)} Y_p^{q*}(\hat{\mathbf{k}})d\hat{\boldsymbol{k}}. \tag{59}$$

We express this integral in spherical coordinates, by substituting

$$\hat{\mathbf{k}} = (\sin(\theta)\cos(\phi), \sin(\theta)\sin(\phi), \cos(\theta)) \tag{60}$$

and the definition of the spherical harmonics in spherical coordinates (44). We then find

$$C_1 C_2 \int_0^{2\pi} e^{\mathrm{i}(s-q)\phi}d\phi \int_0^{\pi} P_r^s(\cos(\theta)) e^{\mathrm{i}kD\cos(\theta)} P_p^q(\cos(\theta))\sin(\theta)d\theta, \tag{61}$$

with

$$\begin{aligned} C_1 &= (-1)^q \left[\frac{(p-q)!}{(p+q)!}\frac{2p+1}{4\pi}\right]^{1/2}, \\ C_2 &= (-1)^s \left[\frac{(r-s)!}{(r+s)!}\frac{2r+1}{4\pi}\right]^{1/2}. \end{aligned}$$

Due to the orthogonality of complex exponentials, only spherical harmonics with the same order interact.

8.4 Rotations

In this section it is shown that the spherical harmonics translation (52) can be decomposed in two $O(S^3)$ rotations and a shift along the z-axis. This decomposition is applied in the context of the low-frequency MLFMA in [34]. We apply it here in the ordinary MLFMA as a means of constructing an efficient scheme with a low sampling rate. Define $\mathbf{D} = \boldsymbol{c}_{m_c}^{l+1} - \boldsymbol{c}_m^l$. Let $\mathbf{R}$ be a rotation matrix such that $\mathbf{R}^T \cdot \mathbf{D} = \mathbf{e}_z$, with $(\cdot)^T$ the transpose and the dot indicating the matrix-vector product. The z-axis is chosen because a shift along the z-axis can be performed in $O(S^3)$ operations, due to the orthogonality of the Fourier basis functions in the definition of the spherical harmonics. We apply the change of variables $\hat{\boldsymbol{k}} \rightarrow \mathbf{R} \cdot \hat{\boldsymbol{k}}$ to the integral in (52) and find

$$\int_{\hat{S}} Y_r^s(\mathbf{R} \cdot \hat{\boldsymbol{k}}) e^{\mathrm{i}k(\mathbf{R}\cdot\hat{\boldsymbol{k}})\cdot\mathbf{D}} Y_p^{q*}(\mathbf{R} \cdot \hat{\boldsymbol{k}}) d(\mathbf{R} \cdot \hat{\boldsymbol{k}}). \tag{62}$$

All areas on the sphere are weighed equally, so that

$$d(\mathbf{R} \cdot \hat{\boldsymbol{k}}) = d\hat{\boldsymbol{k}}. \tag{63}$$

Also, using indicial notation, we can easily derive

$$(\mathbf{R} \cdot \hat{\boldsymbol{k}}) \cdot \mathbf{D} = R_{ij} k_j D_i = R_{ji}^T k_j D_i = k_j R_{ji}^T D_i = \hat{\boldsymbol{k}} \cdot (\mathbf{R}^T \cdot \mathbf{D}). \tag{64}$$

The integral (62) then becomes

$$\int_{\hat{S}} Y_r^s(\mathbf{R} \cdot \hat{\boldsymbol{k}}) e^{\mathrm{i}k\hat{\boldsymbol{k}}\cdot D\mathbf{e}_z} Y_p^{q*}(\mathbf{R} \cdot \hat{\boldsymbol{k}}) d\hat{\boldsymbol{k}}. \tag{65}$$

This shows that any shift can be written as a shift along the z-axis for suitably rotated spherical harmonics. The spherical harmonics $Y_r^s(\hat{\boldsymbol{k}})$ are polynomials of degree r on the unit sphere, with only leading coefficients that are nonzero. This is a property that is invariant under rotations [27]. In fact, the smallest subspaces of continuous functions on the unit sphere invariant under rotations are subspaces of homogeneous polynomials [27]. Spherical harmonics with different degrees therefore do not interact under a rotation, and there exist f_{rs} such that

$$\sum_{s=-r}^{r} Y_r^s(\mathbf{R} \cdot \hat{\mathbf{k}}) f_{rs}' = \sum_{q=-r}^{r} Y_r^q(\hat{\mathbf{k}}) f_{rq}. \tag{66}$$

These can be calculated in the following way

$$f_{rs}' = \sum_{q=-r}^{r} \int_{\hat{S}} Y_r^{s*}(\mathbf{R} \cdot \hat{\mathbf{k}}) Y_r^q(\hat{\mathbf{k}}) d\hat{\mathbf{k}} f_{rq}. \tag{67}$$

An arbitrary spherical harmonics shift can be decomposed into a rotation $\mathbf{R}$, a shift along the z-axis, and the inverse rotation $\mathbf{R}^T$

$$\sum_{q'=-p}^{p} \int_{\hat{S}} Y_p^{q'}(\mathbf{R}\cdot\hat{\mathbf{k}}) Y_p^{q*}(\hat{\mathbf{k}}) d\hat{\mathbf{k}} \sum_{s'=-r}^{r} \int_{\hat{S}} Y_r^{s'}(\mathbf{R}\cdot\hat{\boldsymbol{k}}) e^{\mathrm{i}k\hat{\boldsymbol{k}}\cdot D\mathbf{e}_z} Y_p^{q'*}(\mathbf{R}\cdot\hat{\boldsymbol{k}}) d\hat{\boldsymbol{k}} \int_{\hat{S}} Y_r^{s'*}(\mathbf{R}\cdot\hat{\mathbf{k}}) Y_r^s(\hat{\mathbf{k}}) d\hat{\mathbf{k}} f_{rs}$$

(68)

The rotations do not need to be applied separately for each interaction. In the MLFMA, the number of distinct rotation matrices $\mathbf{R}$ that we need to consider is small, and the spherical harmonics rotation matrices are precomputed. Recursions can be used for these, as well as for the shift along the z-axis matrices [16].

8.5 Motivation

As discussed in Section 7 the sample rate is reduced by a factor of up to eight if the spherical harmonics are used to represent the far field radiation pattern. At the coarser levels we do actually obtain the factor of eight, because Lagrange interpolation is also applied to the three Cartesian components. The reduction in sample rate results in small and dense matrices for the shifts, instead of large and sparse for the k-space representation and Lagrange interpolation. It is expected that this will result in a decrease in the CPU times. More details are given in chapter 9.

8.6 Reconstruction of the k-space samples based on the spherical harmonics coefficients

In this section we discuss the reconstruction of the k-space samples at the integration points based on the spherical harmonics coefficients using the standard algorithm with computational complexity $O(S^3)$ [30]. We describe the algorithm for the scalar case. Let f_{pq} be the spherical harmonics coefficients and suppose that we want to reconstruct the far field radiation pattern

$$f(\theta,\phi) = \sum_{r=0}^{S} \sum_{s=-r}^{r} f_{rs} Y_{rs}(\theta,\phi). \tag{69}$$

We rewrite this in the following way

$$f(\theta,\phi) = \sum_{s=-S}^{S} e^{\mathrm{i}s\phi} \sum_{l=|r|}^{S} f_{rs} P_r^{|s|}(\cos(\theta)). \tag{70}$$

In the first step of the algorithm we compute

$$f^s(\theta_j) = \sum_{l=|r|}^{S} f_{rs} P_r^{|s|}(\cos(\theta_j)), \tag{71}$$

for all Gauss-Legendre points θ_j and all $s = -S, \ldots, S$. This requires $O(S^3)$ operations. In the second step we compute

$$f(\theta_i,\phi_j) = \sum_{s=-S}^{S} e^{\mathrm{i}s\phi_i} f^s(\theta_j), \tag{72}$$

for all integration points (θ_i, ϕ_j). This step scales like $O(S^3)$ but we could accelerate it with the fast Fourier transform.

8.7 Real spherical harmonics

8.7.1 Description of the real spherical harmonics

In this section we discuss the application of real spherical harmonics. It is expected that these will make the implementation more efficient. The real spherical harmonics are given by

$$Y_{lm}(\theta,\phi) = \begin{cases} \sqrt{2}\sqrt{\frac{(2l+1)}{4\pi}\frac{(l-|m|)!}{(l+|m|)!}}P_l^{|m|}(\cos(\theta))\sin(|m|\phi) & \text{if } m<0, \\ \sqrt{\frac{(2l+1)}{4\pi}}P_l^m(\cos(\theta)) & \text{if } m=0, \\ \sqrt{2}\sqrt{\frac{(2l+1)}{4\pi}\frac{(l-m)!}{(l+m)!}}P_l^m(\cos(\theta))\cos(m\phi) & \text{if } m>0. \end{cases} \tag{73}$$

We will show that the real component of the far field radiation pattern of the individual basis functions only consists of real spherical harmonics with even degree. Introduce the notation $f(\hat{\boldsymbol{k}})$ for an arbitrary (scalar) component of the far field radiation patterns. It is easily shown that $f(-\hat{\boldsymbol{k}}) = f(\hat{\boldsymbol{k}})^*$. In the following, we assume $m<0$. The other cases are similar. Let S^+ be one half of the surface of the unit sphere, and S^- the other half. We then find that

$$\begin{aligned} & \int_{\hat{S}} \mathrm{Re}\, f(\hat{\mathbf{k}})P_l^{|m|}(\cos(\theta))\sin(|m|\phi)d\hat{\mathbf{k}} \\ = & \int_{\hat{S}^+} \mathrm{Re}\, f(\hat{\mathbf{k}})P_l^{|m|}(\cos(\theta))\sin(|m|\phi)d\hat{\mathbf{k}} + \int_{\hat{S}^-} \mathrm{Re}\, f(\hat{\mathbf{k}})P_l^{|m|}(\cos(\theta))\sin(|m|\phi)d\hat{\mathbf{k}} \\ = & \int_{\hat{S}^+} \mathrm{Re}\, f(\hat{\mathbf{k}})P_l^{|m|}(\cos(\theta))\sin(|m|\phi)d\hat{\mathbf{k}} + \int_{\hat{S}^+} \mathrm{Re}\, f(\hat{\mathbf{k}})P_l^{|m|}(\pi-\cos(\theta))\sin(|m|(\phi+\pi))d\hat{\mathbf{k}} \\ = & \int_{\hat{S}^+} \mathrm{Re}\, f(\hat{\mathbf{k}})P_l^{|m|}(\cos(\theta))\sin(|m|\phi)d\hat{\mathbf{k}} + \int_{\hat{S}^+} \mathrm{Re}\, f(\hat{\mathbf{k}})(-1)^{l+|m|}P_l^{|m|}(\cos(\theta))(-1)^{|m|}\sin(|m|(\phi))d\hat{\mathbf{k}}. \end{aligned}$$

It can easily be seen that the above becomes zero for l odd. Using a similar argument it can be shown that the imaginary part becomes zero for l even. This argument cannot be extended to the far field radiation patterns of clusters, because in these we multiply the basis functions by complex surface current expansion coefficients.

8.7.2 Motivation for the use of real spherical harmonics

8.7.2.1 Reduced CPU times for the summation step

The use of real spherical harmonics is expected to result in smaller CPU times for the summation step, described in Section 7.1 for the complex spherical harmonics. Recall that in the summation step the spherical harmonics coefficients of the far field radiation patterns of the clusters at the finest level are computed by summation of the spherical harmonics coefficients of the far field radiation patterns of the individual basis functions. There are two reasons for the lower CPU times if the real spherical harmonics are used:

- The spherical harmonics coefficients of the far field radiation patterns of the individual basis functions at the finest level are purely real for r even and purely imaginary for r odd if the real spherical harmonics are used. The multiplication of a real or imaginary number by a complex number (the surface current expansion coefficient) requires two flops. On the other hand, if the complex spherical harmonics are used then the spherical harmonics coefficients of the far field radiation patterns of the individual basis functions at the finest level are complex. The multiplication of two complex number requires four flops. A very simple estimate then is that the CPU time cost of the matrix-vector product corresponding to the summation step is reduced by a factor 2.
- We do not need to expend flops on reconstructing the spherical harmonics coefficients of the far field radiation patterns of the individual basis functions for negative s if the real spherical harmonics are used. The real spherical harmonics coefficients are all stored permanently in the computer memory.

For both of these reasons we expect that CPU times are lower for the summation step if real spherical harmonics are used.

8.7.2.2 Reduced CPU times for the rotations

If the complex spherical harmonics are used, then the matrix that applies a rotation of the coordinate system to a spherical harmonics expansion is complex. If the real spherical harmonics are used, it is real. The CPU time of the matrix-vector product is then expected to decrease by a factor of two.

8.7.2.3 Reduced CPU times for the reconstruction of the k-space samples at the integration points

The second matrix in Section 8.6 is real if the real spherical harmonics are used, and complex if the complex spherical harmonics are used. The CPU time of the matrix-vector product is then expected to decrease by a factor of two, if the real spherical harmonics are used.

8.8 Interpolation error in spherical harmonics based aggregation

Due to the truncation of the spherical harmonics expansion at $r = S_{l+1}$ the spherical harmonics expansion coefficients $\mathbf{f}_{pq}^{m,l}$ computed using the direct spherical harmonics shift in (52) are only approximately equal to the spherical harmonics coefficients of the exact far field radiation patterns $\sum_{j \in G_m^{\mathrm{b},l}} \int_S \boldsymbol{f}_j e^{\mathrm{i}k\hat{\boldsymbol{k}}\cdot(\boldsymbol{r}-\boldsymbol{c}_m^l)} d\boldsymbol{r}$. The reconstructed k-space samples at the directions $\hat{\boldsymbol{k}}_j^l$ are therefore not equal to the exact k-space samples. We can see this error as an interpolation error.

More specifically, define

$$\sqrt{\int_S \sum_{j\in G_m^{\mathrm{b},l}} \int_S \boldsymbol{f}_j e^{\mathrm{i}k\hat{\boldsymbol{k}}\cdot(\boldsymbol{r}-\boldsymbol{c}_m^l)} d\boldsymbol{r} - \sum_{p=0}^{S_l}\sum_{q=-p}^{p} |\mathbf{f}_{pq}^{m,l} Y_p^q(\hat{\mathbf{k}})|^2 d\hat{\mathbf{k}}} \tag{74}$$

as the interpolation error.

The interpolation error in spherical harmonics based aggregation is due to the finite sample rate and is inherent in the aggregation process. Due to the low sample rate ($S_l = P_l/2$) we use, the interpolation error is of the same order of magnitude as the truncation error due to the finite number of multipoles in the transfer function. The finite sample rate as such also results in a small contribution to the interpolation error in the standard MLFMA. However, due to the larger sample rate in the standard MLFMA its contribution is dwarfed by the error due to the use of a local interpolator. In fact, if a global interpolator such as [9] is used in the MLFMA with the conventional oversampling where the number of directions K_l is equal to the number of integration points, then the interpolation error will become much smaller. The interpolation in the standard MLFMA with Lagrange interpolation can also be made smaller by using a larger interpolation stencil. In contrast, we can only reduce the interpolation error in spherical harmonics based aggregation by increasing the sample rate.

Consider the MLFMA where the k-space representation is used in conjunction with a global interpolator and the usual oversampling. In the following we will argue that the finite sample rate as such results in a small interpolation error and compare it to spherical harmonics based aggregation. Suppose that we have a spherical harmonics expansion $\sum_{r=0}^{S_1}\sum_{s=-r}^{r} f_{rs} Y_r^s(\hat{\mathbf{k}})$, with S_1 as yet unknown, of the far field radiation pattern at level $l+1$. This is the result of using a global interpolator such as [9], instead of a local interpolator for interpolating the far field radiation patterns. The S_1 will be determined in this analysis. We apply the shift operator $e^{\mathrm{i}k\hat{\boldsymbol{k}}\cdot(\boldsymbol{c}_{m_c}^{l+1}-\boldsymbol{c}_m^l)}$ to it in the k-space representation. The k-space samples $\boldsymbol{v}_{m,l}^{(o)}$ at the directions $\hat{\boldsymbol{k}}_j^l$ are then actually samples of the function $\sum_{m_c\in G_m^l} e^{\mathrm{i}k\hat{\boldsymbol{k}}\cdot(\boldsymbol{c}_{m_c}^{l+1}-\boldsymbol{c}_m^l)} \sum_{r=0}^{S_1}\sum_{s=-r}^{r} f_{rs} Y_r^s(\hat{\mathbf{k}})$. We argue, that if global interpolation is used, we will only be able to recover spherical harmonics coefficients up to a certain degree S_2, depending on the number K_l of directions $\hat{\boldsymbol{k}}_j^l$ of the above expression. This parameter we could the implicit spherical harmonics truncation parameter in the standard MLFMA. Recall that at level l we use $K_l = 2P_l^2$ directions. We will see that this is sufficient only to reproduce spherical harmonics coefficients up to degree P_l. Remember that spherical harmonics coefficients are defined by

$$f_{pq} = \int_{\hat{S}} f(\hat{\boldsymbol{k}}) Y_p^{q*}(\hat{\boldsymbol{k}}) d\hat{\boldsymbol{k}}, \tag{75}$$

If f is a band-limited function containing only spherical harmonics coefficients up to degree P_l then the integrand is a polynomial of maximum degree $2P_l$ and $K_l = 2P_l^2$ directions are

sufficient for exact numerical integration, see Section 6.3.1. We then find that $S_1 = P_{l+1}$ and $S_2 = P_l$ is consistent with the MLFMA aggregation process. In practice, the far field radiation patterns are not exactly band-limited, and there will be a numerical integration error due to the higher-degree terms whose analytical integral is zero, but whose numerical integral is nonzero. In summary, if the k-space representation is used, then spherical harmonics coefficients up to degree P_l are implicit in the data. If the direct spherical harmonics shifts are used with a truncation parameter of $\frac{P_l}{2}$, then only spherical harmonics up to degree $\frac{P_l}{2}$ are stored. There is hence a larger error due to the finite sample rate in spherical harmonics based interpolation, but there is no error due to the use of a local interpolator.

As a test of the effect of the truncation of the spherical harmonics expansion on the interpolation error we compute the far field radiation patterns at the next-to-finest level $l = l_{\text{max}-1}$. We do not give details about the shape mesh, but note that we computed the error at a curved part of the mesh. The cube diameter at the finest level is $d_c = 0.2\lambda$. We use the notation $\tilde{f}(\hat{\mathbf{k}})$ for the reconstructed far field radiation pattern and the notation $f(\hat{\mathbf{k}})$ for the exact far field radiation pattern. We are interested in the relative error

$$\epsilon = \frac{\max_{\hat{\mathbf{k}}} |\tilde{f}(\hat{\mathbf{k}}) - f(\hat{\mathbf{k}})|}{\max_{\hat{\mathbf{k}}} |f(\hat{\mathbf{k}})|}. \tag{76}$$

We compute ϵ for the truncation parameters $S_{l_{\text{max}}} = \frac{P_{l_{\text{max}}}}{2}, 2\frac{P_{l_{\text{max}}}}{2}, 3\frac{P_{l_{\text{max}}}}{2}$, where the factor in front of the quotients is given on the horizontal axis in Figure 7. The number of multipoles is given by $P_{l_{\text{max}}} = 7$ at the finest level, and $P_{l_{\text{max}-1}} = 11$ at the next-to-finest level. Furthermore, we round off the quotients to above, so that $S_{l_{\text{max}}} = 4$ and $S_{l_{\text{max}-1}} = 6$. The relative error ϵ is given on the vertical axis. For comparison, we also compute the far field radiation patterns using Lagrange interpolation with $K_{l_{\text{max}}} = 2(P_{l_{\text{max}}})^2, 2(2P_{l_{\text{max}}})^2, 2(3P_{l_{\text{max}}})^2$ directions and a stencil of ninterp $= 6, 8, 10, 12, 14$ points in the two-step Lagrange interpolation process. The sample rate is hence smaller by a factor of eight in the tests with the spherical harmonics shifts. As the truncation parameter $S_{l_{\text{max}}}$ is increased, the relative error decreases exponentially. It can be shown that the terms in the spherical harmonics shift matrix decay super-exponentially as $r \to \infty$, see Appendix A. Also, the spherical harmonics coefficients of the far field radiation patterns themselves decay super-exponentially.

A question that remains is what the effect of the interpolation error is on the whole algorithm. Consider the error in (52) due to the truncation of the spherical harmonics expansion. We have that

$$\sum_{r=S_{l+1}+1}^{\infty} \sum_{s=-r}^{r} |\mathbf{f}_{rs}^{m_c,l+1}|^2 = \sum_{r=S_{l+1}+1}^{\infty} \sum_{s=-r}^{r} |\mathbf{f}_{rs}^{m_c,l+1} Y_r^s(\hat{\mathbf{k}})|^2. \tag{77}$$

Note that the above spherical harmonics coefficients are not actually computed in the algorithm.

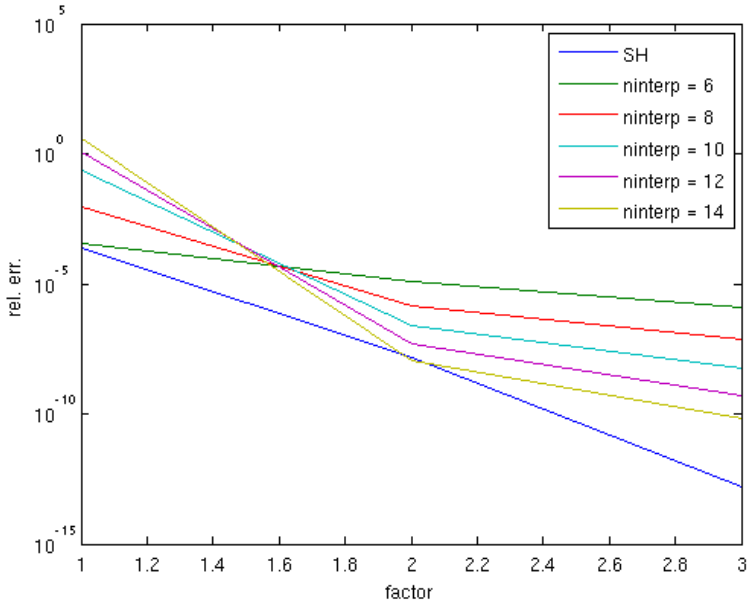

Fig. 7 Relative error in the far field radiation patterns

The shift $e^{\mathrm{i}k\hat{\boldsymbol{k}}_j^l\cdot(\boldsymbol{c}_{mc}^{l+1}-\boldsymbol{c}_m^l)}$ is a unitary (norm-preserving) operator and will conserve this error into the next, coarser level, where it will affect all the computed spherical harmonics coefficients. Of course, part of the error will be present in spherical harmonics with degree $p > S_l$ and the errors from multiple clusters and levels may cancel each other out. But generally, the effect of the interpolation error on the aggregated far field radiation patterns can be estimated by summing over the the above errors for all clusters and levels. We have verified that the error in the reconstructed outgoing waves remains below $\epsilon < 0.001$ for three levels in an arbitrary surface mesh if the spherical harmonics expansions are truncated at $S_l = \frac{P_l}{2}$.[1]

9 Computational complexity and memory requirements

9.1 Memory requirements

The memory requirements are dominated by the costs of storing the spherical harmonics coefficients of the far field radiation patterns of each individual basis functions at the finest level

$$\mathbf{f}_{rs}^{j,m_{l_{\max}}} := \int_{\hat{S}} \boldsymbol{v}_{j,l_{\max}+1}^{(o)}(\hat{\boldsymbol{k}}) Y_r^{s*}(\hat{\boldsymbol{k}}) d\hat{\boldsymbol{k}}. \tag{78}$$

[1] At higher levels it was problematic to compute the exact far field expansions.

These are used in the summation step, described in Section 7.1. The aggregation phase does not require much memory, because a small set of matrices is used repeatedly for many different groups. The number of spherical harmonics coefficients we need to store at the finest level is given by

$$N(S_{l_{\max}}+1)^2. \tag{79}$$

As discussed in Section 8.7.2 the spherical harmonics coefficients are purely real for r even and purely imaginary for r imaginary. This is a structure that we can exploit in implementations.

9.2 Estimates for the CPU times for the aggregation phase

In this section estimates based on a simple model for the CPU costs are given for both Lagrange interpolation and the new method. The CPU costs are estimated by counting the number of nonzero entries in the matrices that implement these methods.

Rotations of spherical harmonics expansions are implemented by block diagonal matrices. The block corresponding to degree i collects the nonzero interactions between the spherical harmonics coefficients, with orders up to i. The number of nonzero entries N_R in the rotation matrix is

$$N_R = \sum_{i=0}^{S}(2i+1)^2 = \frac{4S^3}{3} + 4S^2 + \frac{16S}{6}. \tag{80}$$

The rotation matrices are real if real spherical harmonics are used (see Section 8.7.2) so we are performing matrix-vector products with real matrices and complex vectors, so that two flops are required for each entry in the matrix.

We will now estimate the number of nonzero entries in the matrix that shifts the spherical harmonics expansion along the z-axis. This is also called the coaxial shift matrix in the literature. The block corresponding to order i collects the nonzero interactions between spherical harmonics coefficients, with degree equal to or larger than i. The number of nonzero entries N_T in the coaxial shift matrix is

$$N_T = (S+1)^2 + 2\sum_{i=1}^{S}(S-i+1)^2 = \frac{2S^3}{3} + 2S^2 + \frac{7S}{3} + 1. \tag{81}$$

The entries of the coaxial shift matrix are either purely real or purely imaginary. We do not expect that it is convenient to implement this structure, so we will implement this matrix as a complex matrix. A matrix-vector product with a complex matrix and a complex vector quires four flops for each entry of the matrix. Since all other matrices in this analysis require two flops per entry, we will count each entry in the coaxial shift matrix twice in our estimate of the number of nonzero entries.

Recall that a general translation can be decomposed into a rotation, a shift along the z-axis, and the inverse rotation. Between the shift along the z-axis and either of the rotations the spherical harmonics coefficients are permuted so that the ordering is by degree for the rotations and by order for the shift along the z-axis. We neglect the CPU cost of applying the permutations in this estimate. We obtain the following estimate for the total number of nonzero entries

$$N_{\text{tot}}^{\text{SH}} = 2N_R + 2N_T = 4S^3 + 12S^2 + 10S + 2, \tag{82}$$

where each entry in the coaxial shift matrix has been counted twice because it has been implemented as a complex matrix.

We will now estimate the number of nonzero entries in the matrices implementing Lagrange interpolation. As mentioned in Section 6.2 we use a two-step process for the Lagrange interpolation. In the first step we determine interpolations $\tilde{f}_1(\phi, \theta_i)$, separately for all values of θ_i corresponding to directions at the previous level, and we evaluate the interpolations at all the $\phi = \phi_j$ corresponding to target points at the new level. In the second step we determine interpolations $\tilde{f}_2(\phi_j, \theta)$, separately for all values of ϕ_j corresponding to target points at the new level, and we evaluate the interpolations at the target points $\theta = \theta_l$ corresponding to the new level. It can be seen that the number of nonzero entries depends on the number of multipoles at both the previous and the new level. For simplicity, we estimate the number of nonzero entries for an interpolation where the number of multipole terms is the same at the previous and new level. This is actually a small overestimate of the number of nonzero entries in the actual aggregation process in the MLFMA, where the number of multipoles is smaller at the previous level. In both interpolations we use a stencil of 6 points. Recall that the number of directions on the unit sphere is given by

$$K = 2P^2. \tag{83}$$

Also, remember that S has been chosen so that $P = 2S$. The total number of nonzero entries in the two interpolation matrices can then be estimated by

$$N_{\text{tot}}^{\text{Lagrange}} = 12K. \tag{84}$$

The CPU costs of applying the phase shift factors $e^{\mathrm{i}k\hat{\boldsymbol{k}}_j^l \cdot (\boldsymbol{c}_{m_{l+1}}^{l+1} - \boldsymbol{c}_{m_l}^l)}$ have been neglected in this analysis. The estimates for the CPU costs are plotted in Figure 8. It can be seen that the CPU costs are lower for new method if the number of multipoles P is smaller than about 40.

Note that counting the number of nonzero entries is not a perfect way of estimating the CPU costs. The Lagrange interpolation matrices are large and sparse, whereas the matrices for the new method are small and block diagonal with dense blocks. If the number of nonzero entries is the same, it is expected that the new method is faster due to more efficient implementations.

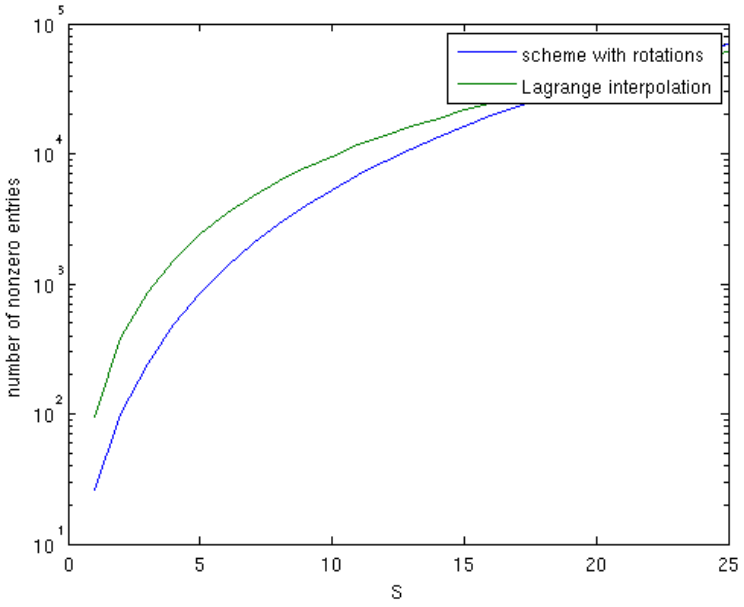

Fig. 8 Estimates of the number of nonzero entries in the matrices implementing the methods in this report. We intend to switch to Lagrange interpolation with the parallellization strategy over the wave directions at values of S between 15 and 50, but the details still have to be worked out.

9.3 Estimate for the CPU cost of the reconstruction of the k-space samples based on the spherical harmonics coefficients

In this section we estimate the number of nonzero entries in the matrices implementing the reconstruction of the k-space samples from the spherical harmonics expansion

$$f(\theta_i, \phi_j) = \sum_{r=0}^{S} \sum_{s=-r}^{r} f_{rs} Y_r^s(\theta_i, \phi_j), \tag{85}$$

for a scalar function f with spherical harmonics coefficients f_{rs}. See Section 8.6 for a description of the algorithm. In the first step we compute

$$f^s(\theta_i) = \sum_{r=|s|}^{S} f_{rs} P_r^{|s|}(\cos(\theta_i)), \tag{86}$$

for all Gauss-Legendre points θ_i and all $s = -S, \ldots, S$. Recall that in the fast multipole method, the integration points have been chosen so that the k-space integrals (37) are integrated accurately, with P distinct values of θ_i. Also, remember that S has been chosen so that $P = 2S$. It can be seen that for any s we need to compute a sum with $S - s + 1$ terms. This step can be

implemented with a real matrix of dimensions $2S^2 \times (S+1)^2$ containing

$$N_1 = 2S(2\sum_{s=1}^{S}(S-s+1)+S+1) = 2S^3+4S^2+2S. \tag{87}$$

nonzero entries. If the complex spherical harmonics are used, then in the second step we compute

$$f(\theta_i,\phi_j) = \sum_{s=-S}^{S} e^{\mathrm{i}s\phi_j} f^s(\theta_i), \tag{88}$$

for all integration points (θ_i,ϕ_j). There are $2P = 4S$ distinct values of ϕ_j. This step can be implemented with a $8S^2 \times 2S^2$ matrix containing

$$N_2 = \underbrace{2S}_{\theta_i\text{-values}}\ \underbrace{4S}_{\phi_j\text{-values}}\ \underbrace{(2S+1)}_{\text{sum over } s} = 16S^3+8S^2. \tag{89}$$

entries. This step can be accelerated with the fast Fourier transform. If the complex spherical harmonics are used then this matrix is complex. The corresponding matrix for the real spherical harmonics also contains $2S4S(2S+1)$ entries and is real. The total number of nonzero entries in the matrices implementing the reconstruction of k-space samples from the spherical harmonics expansion is then

$$N_{\text{tot}}^{\text{reconstruction}} = N_1+N_2 = 18S^3+12S^2+2S. \tag{90}$$

It is seen that this is considerably more than for a single shift (see (82)). We do not, however, expect that this is problematic for the method. Recall that for any cluster at some level we only need to apply the reconstruction once, but it contains up to eight subclusters. This means that we need to apply up to eight shifts of the coordinate system (in the case of spherical harmonics based aggregation) or Lagrange interpolations per cluster at this level. Therefore the efficiency of this step is less critical than the efficiency of the shifts and rotations if spherical harmonics based aggregation is applied. Also, the most expensive second step can be accelerated with the fast Fourier transform. In summary, we see that the reconstruction of the k-space samples from the spherical harmonics expansion can be performed efficiently.

9.4 Estimates for the CPU cost if the rotations are not used

In this section we estimate the number of nonzero entries in the matrix implementing a general shift of the coordinate system (52), if the decomposition into a rotation, coaxial shift, and inverse rotation is not used. In a general shift (in other words, not along the z-axis), all the spherical harmonics coefficients interact with each other. The number of nonzero entries in the matrix then is

$$(S+1)^4. \tag{91}$$

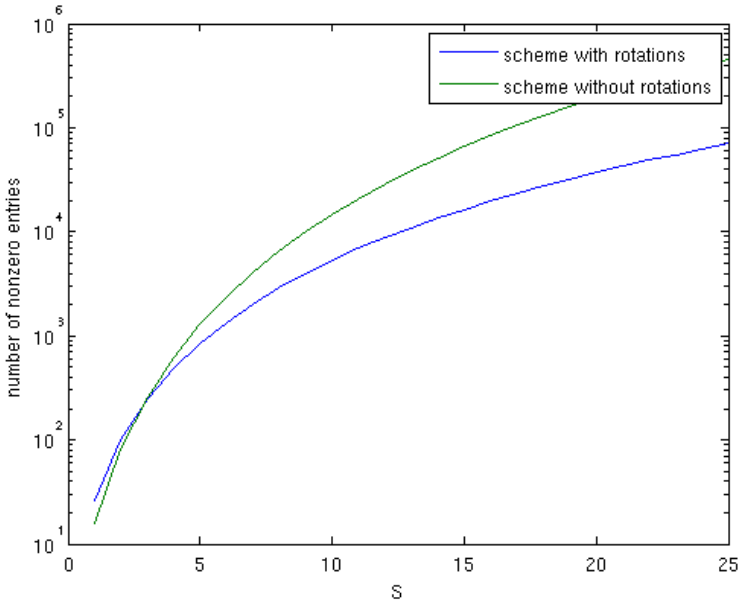

Fig. 9 Estimates of the number of nonzero entries in the matrices implementing the methods with and without rotations.

If the real spherical harmonics are used then the entries of this matrix are either completely imaginary or completely real. Even if we succeed in implementing this structure, this scheme will not be competitive, as can be seen in Figure 9. The number of nonzero terms is much larger than for the scheme with rotations.

9.5 CPU time measurements

In this section we give CPU time measurements for Lagrange interpolation and spherical harmonics based aggregation with real spherical harmonics. As mentioned, this technique is based on a decomposition of the matrix for general shifts $\mathbf{d}$ into a rotation, a coaxial shift, and the inverse rotation. Between the coaxial shift and the rotations the spherical harmonics coefficients are permuted so that they are ordered by degree for the rotations, and by order for the shift along the z-axis. We have implemented the new scheme in Fortran. We ran into a slight delay in the implementation of the rotation matrices. Therefore we have only measured the costs of the permutations and the coaxial shift, for a shift along the z-axis $\mathbf{d} = d\mathbf{e}_z$. We have also not tested CPU times for the reconstruction of the k-space samples based on the spherical harmonics coefficients. We do remark that for each group at the coarser level up to eight general shifts from the finer to the coarser level need to be performed, and we only apply the reconstruction of the k-space samples a single time. The rotation matrix has a structure similar to the coaxial shift matrix, so expect the total CPU time for a general shift to be larger by a factor of at most 3. Fur-

S	5	10	15
CPU time (s) for new technique	0.0424	0.0454	0.0858
CPU time (s) for Lagrange interpolation	1.37	1.44	3.08

Table 2 CPU time measurements for the technique based on rotations and Lagrange interpolation. The truncation parameter S corresponds to $P = 2S$ multipole terms in the transfer function.

thermore, the computations with the new technique were performed with a real surface current expansion coefficient vector. In general, this vector is complex, which will require about two times as many computations. We hence expect that the CPU times for the new technique will be about six times as large in the complete algorithm. The matrix-vector products have been implemented using the BLAS library, and the permutations have been implemented using a do-loop. We compare the CPU times with the existing implementation using Lagrange interpolation. The CPU times reported are for 10000 repeated applications of the method. The results are given in Table 9.5. It can be seen that the new scheme results in a considerable reduction in CPU time.

10 Possible further improvements

In this section we discuss possibilities extending spherical harmonics based aggregation to computational complexity better than $O(P^3)$, a low sample rate, and efficient implementations. We expect that this is difficult.

The coaxial shift can easily be performed using a method with computational complexity better than $O(P^3)$ and a low sample rate, but it appears to be hard to implement it efficiently. The spherical harmonics coefficients after a coaxial shift are given by

$$f'_{pq} = \int_{\hat{S}} Y_p^{q*}(\hat{\mathbf{k}}) e^{\mathrm{i}k\hat{\mathbf{k}}\cdot\hat{\mathbf{e}}_z d} \sum_{r=0}^{S} \sum_{s=-r}^{r} f_{rs} Y_r^s(\hat{\mathbf{k}}) d\hat{\mathbf{k}}. \tag{92}$$

We know that only interactions between spherical harmonics coefficients with the same order are nonzero. We then find the following expression for the nonzero interactions

$$f'_{pq} = \int_0^{\pi} P_p^q(\cos(\theta)) e^{\mathrm{i}kd\cos(\theta)} \sum_{r=|q|}^{S} C_{rq} f_{rq} P_r^q(\cos(\theta)) d\theta, \tag{93}$$

with C_{rq} constant factors. The idea is to compute this integral numerically during the solution phase of the algorithm, instead of during the initialization phase, in contrast to the technique that we have examined up to now. The computations are split over three steps:

evaluation of the expansion at the Gauss-Legendre quadrature points θ_i

$$f(\theta_i) := \sum_{r=|q|}^{S} C_{rq} f_{rq} P_r^q(\cos(\theta_i)).$$

This operation has computational complexity $0(S^2)$ if performed directly. This expansion also appears in $0(S^3)$ algorithms for spherical harmonic transforms and there is an extensive literature about accelerating it to a better computational complexity.

shift where we compute

$$g(\theta_i) := e^{\mathrm{i}kd\cos(\theta_i)} f(\theta_i).$$

This operation has computational complexity $O(S)$.

computation of the coefficients

$$\sum_{i=1}^{K_\theta} \omega_i^{\mathrm{GL}} P_p^q(\cos(\theta_i)) g(\theta_i),$$

with ω_i^{GL} the Gauss-Legendre weights. This operation has computational complexity $O(S^2)$ if performed directly. This expansion also appears in $0(S^3)$ algorithms for inverse spherical harmonic transforms and there is an extensive literature about accelerating it to a better computational complexity.

In principle we now end up with an algorithm for coaxial shifts that has a low sample rate and a better computational complexity. The problem is that it is hard to implement fast (with a better computational complexity) algorithms for the above expansions efficiently. For example, in a recent paper [19] an $O(S(\log S)^2/\log\log S)$ algorithm is described for computing sums of the form $\sum_{r=0}^{S} f_{r0} P_r^0(\cos(\theta_i))$, which is a special case of the problem we are concerned with. The fast algorithm only outperforms the direct method for $S > 1000$. These values of S are only relevant for radar-cross section computations with very high frequencies and for these S we will use Lagrange interpolation with the parallellization strategy over the clusters and not spherical harmonics based aggregation.

Accelerating the rotations to a better computational complexity and a low sample rate is more difficult. We have examined an algorithm similar to those in [14] and [26]. It is known that any rotation can be decomposed into a rotation along the z-axis, a rotation along the y-axis, and another rotation along the z-axis, using the Euler angles. Only the rotation matrix along the y-axis has dense blocks. Any rotation can be decomposed in such a way that only rotations along the y-axis with angles $\pi/2$ are required [28]. Recall that the rotated spherical harmonics coefficients are given by

$$f'_{rs} = \sum_{q=-r}^{r} f_{rq} \int_{\hat{S}} Y_r^{s*}(\mathbf{R}\cdot\hat{\mathbf{k}}) Y_r^q(\hat{\mathbf{k}}) d\hat{\mathbf{k}}. \tag{94}$$

We rewrite this to

$$f'_{rs} = \int_{\hat{S}} Y_r^{s*}(\hat{\mathbf{k}}) \sum_{q=-r}^{r} f_{rq} Y_r^q(\mathbf{R}^T \cdot \hat{\mathbf{k}}) d\hat{\mathbf{k}}. \tag{95}$$

We apply a quadrature with evenly-spaced points $(\phi_i, 0)$ on the Equator. We then find that we need to evaluate a sum of the form

$$\sum_{q=-r}^{r} f_{rq} Y_r^q(\frac{\pi}{2}, \cos(\frac{2k-1}{2n}\pi)), \tag{96}$$

with k an index and n the number of points. Note that the expansion is now over the order, and that it is evaluated at the Chebyshev points. This method is ill-conditioned, but that can be solved by adding a few points off the Equator, as discussed in [26] for a similar technique.
We think that standard methods for accelerating the expansion $\sum_{r=|q|}^{S} f_{rq} P_r^q(\cos(\theta_i))$ cannot be applied to expansions over the order. The standard technique for evaluating the expansion over the degree is based on expressing the Legendre polynomials up to some degree as a linear combination of Chebyshev polynomials up to the same degree [30]. The matrix expressing this linear map is smooth away from the main diagonal. This is a consequence of the fact that the Legendre polynomials and Chebyshev polynomials are defined using similar recursive relations. A fast multipole method is then applied to accelerate the transform from the Legendre coefficients to the Chebyshev coefficients [4]. The Chebyshev polynomials can be evaluated at the Chebyshev points using the fast Fourier transform.
Unfortunately, the associated Legendre polynomials with odd orders are not actually polynomials, and we cannot express them as a finite linear combination of Legendre polynomials. Also, the recursion over the order defining the associated Legendre polynomials for a given degree is strongly different from the recursion over the degree defining the Legendre polynomials. Therefore, we expect that the standard techniques for obtaining a fast transform cannot be extended to the sums (96).
In [17] and [33] an alternative technique for accelerating the rotations is described, where the rotation matrix is decomposed into a product of diagonal and Toeplitz/Hankel matrices. The authors encountered difficulties with efficiently implementing the methods. In summary, we think that methods with better computational complexity are not efficient for the values of S where we use the spherical harmonics based aggregation, and not Lagrange interpolation with the parallellization strategy over the clusters.

11 Conclusion

The standard method for the aggregation of far fields in the ordinary MLFMA is Lagrange interpolation. In this report we have examined a new method, where the far field radiation patterns are represented by real spherical harmonics, instead of the k-space values. The effect of rotations and shifts on the expansion coefficients is computed directly, and the far field radiation patterns are only reconstructed for the application of the transfer function.

The advantage of the new method is that it has a sample rate that is lower by a factor of up to 8 compared to Lagrange interpolation. It is hoped that this will result in lower CPU times at the finer levels, where the number of multipoles is low. Preliminary tests with low P indicate that CPU times are reduced by factors of about 30. We did not test all the steps of the algorithm, but based on these results we expect that CPU times are reduced by about 5 at the finer levels with low P (of the order $O(10)$) in the complete algorithm.

The method has two disadvantages:

- The computational complexity is $O(P^3)$, compared to $O(P^2)$ for Lagrange interpolation.
- It can only be parallellized over the clusters and this will limit the number of parallel processes at the higher levels.

For both of these reasons it is important to shift to Lagrange interpolation at the coarser levels with large clusters.

We also want to make a remark about the application of the method. The spherical harmonics based aggregation is expected to perform well at small values of P. The values of P prescribed by the excess bandwidth formula (43)

$$P = kd + 1.8 d_0^{2/3} (kd)^{1/3}, \tag{97}$$

are particularly low for levels with $d < \lambda$, and this was our initial motivation for developing the new method based on rotations. These are also the values for which we have reported CPU times. However, our tests have indicated that the relative error in the multipole approximation to the Green's function is not smaller than $\epsilon = 0.001$ if we use the excess bandwidth formula at levels with $d < \lambda$. In fact, due to the low-frequency breakdown the FMM approximation is not exactly controllable to this precision at levels with small d. On the other hand, this formula has been used for a long time at the National Aerospace Laboratory for these parameter values, and the accuracy in the solution that is calculated by the FMM is good.

A number of things still remain to be done. We still need to determine the precise level at which it becomes better to switch to Lagrange interpolation. We have also not yet performed integral tests of the MLFMA with the new aggregation algorithm, by measuring the error in the solution.

This page is intentionally left blank.

Appendix A Convergence of direct spherical harmonics translations

In this chapter we show that the spherical harmonics translation error decays super-exponentially as $r \to \infty$ in (52). The entries of the spherical harmonics translation matrix are given by

$$\int_{\hat{S}} Y_{rs}(\hat{\boldsymbol{k}}) e^{\mathrm{i}k\hat{\boldsymbol{k}}\cdot\mathbf{D}} Y^*_{pq}(\hat{\boldsymbol{k}}) d\hat{\boldsymbol{k}}. \tag{98}$$

In this section, we consider the case where $\mathbf{D} = D\mathbf{e}_z$. But first, we apply a spherical harmonics expansion to the exponential factor

$$\int_{\hat{S}} Y_{rs}(\hat{\boldsymbol{k}}) \sum_{\nu=0}^{\infty} \mathrm{i}^{\nu}(2\nu+1) j_{\nu}(kD) P_{\nu}(\hat{\boldsymbol{k}}\cdot\hat{\mathbf{D}}) Y^*_{pq}(\hat{\boldsymbol{k}}) d\hat{\boldsymbol{k}}. \tag{99}$$

We continue

$$\int_{\hat{S}} Y_{rs}(\hat{\boldsymbol{k}}) \sum_{\nu=0}^{\infty} \mathrm{i}^{\nu}(2\nu+1) j_{\nu}(kD) \frac{4\pi}{2\nu+1} \sum_{\mu=-\nu}^{\nu} Y^*_{\nu\mu}(\hat{\mathbf{D}}) Y_{\nu\mu}(\hat{\boldsymbol{k}}) Y^*_{pq}(\hat{\boldsymbol{k}}) d\hat{\boldsymbol{k}}. \tag{100}$$

These expansions were taken from [25]. Rearranging, we find

$$4\pi \sum_{\nu=0}^{\infty} \mathrm{i}^{\nu} j_{\nu}(kD) \sum_{\mu=-\nu}^{\nu} Y^*_{\nu\mu}(\hat{\mathbf{D}}) \int_{\hat{S}} Y_{rs}(\hat{\boldsymbol{k}}) Y_{\nu\mu}(\hat{\boldsymbol{k}}) Y^*_{pq}(\hat{\boldsymbol{k}}) d\hat{\boldsymbol{k}}. \tag{101}$$

We now apply the identities [1]

$$Y^*_{pq}(\hat{\boldsymbol{k}}) = (-1)^q Y_{p,-q}(\hat{\boldsymbol{k}}), \tag{102}$$

and [2]

$$\int_{\hat{S}} Y_{rs}(\hat{\boldsymbol{k}}) Y_{\nu\mu}(\hat{\boldsymbol{k}}) Y_{p,-q}(\hat{\boldsymbol{k}}) d\hat{\boldsymbol{k}} = \sqrt{\frac{(2r+1)(2\nu+1)(2p+1)}{4\pi}} \begin{pmatrix} r & \nu & p \\ 0 & 0 & 0 \end{pmatrix} \begin{pmatrix} r & \nu & p \\ s & \mu & -q \end{pmatrix}, \tag{103}$$

with $\begin{pmatrix} j_1 & j_2 & j_3 \\ m_1 & m_2 & m_3 \end{pmatrix}$ the Wigner 3-j symbols. We then find

$$2\sqrt{\pi} \sum_{\nu=0}^{\infty} \mathrm{i}^{\nu} j_{\nu}(kD) \sum_{\mu=-\nu}^{\nu} Y^*_{\nu\mu}(\hat{\boldsymbol{D}}) \sqrt{(2r+1)(2\nu+1)(2p+1)} \begin{pmatrix} r & \nu & p \\ 0 & 0 & 0 \end{pmatrix} \begin{pmatrix} r & \nu & p \\ s & \mu & -q \end{pmatrix}. \tag{104}$$

Now we will make of the following properties of Wigner 3-j symbols [2]. A Wigner 3-j symbol $\begin{pmatrix} j_1 & j_2 & j_3 \\ m_1 & m_2 & m_3 \end{pmatrix}$ is nonzero only if

$$m_1 + m_2 + m_3 = 0, \tag{105}$$

$$|j_1 - j_2| \leq j_3 \leq j_1 + j_2. \tag{106}$$

We first apply condition (105) to find $\mu = q - s$. We will also make use of the following property

$$\begin{pmatrix} j_1 & j_2 & j_3 \\ m_1 & m_2 & m_3 \end{pmatrix} = \begin{pmatrix} j_3 & j_1 & j_2 \\ m_3 & m_1 & m_2 \end{pmatrix}. \tag{107}$$

Using this property and (106) we find that

$$|p - r| \leq \nu \leq p + r. \tag{108}$$

Applying these results in (104) we find

$$2\sqrt{\pi} \sum_{\nu=\max\{|q-s|,|p-r|\}}^{p+r} \mathrm{i}^{\nu} j_{\nu}(kD) Y^{*}_{\nu,q-s}(\hat{\boldsymbol{D}}) \sqrt{(2r+1)(2\nu+1)(2p+1)} \begin{pmatrix} r & \nu & p \\ 0 & 0 & 0 \end{pmatrix} \begin{pmatrix} r & \nu & p \\ s & q-s & -q \end{pmatrix}. \tag{109}$$

We will now make use of the fact that $\mathbf{D} = D\mathbf{e}_z$. The point $\mathbf{e}_z$ corresponds to the point $(0, \phi)$, with ϕ indeterminate, in spherical coordinates. We write out the definition of the spherical harmonics

$$Y^{*}_{\nu,q-s}(\mathbf{e}_z) = (-1)^{q-s} \left[\frac{(\nu - (q-s))!}{(\nu + (q-s))!} \frac{2\nu+1}{4\pi} \right]^{1/2} P_{\nu}^{q-s}(\cos(0)) e^{-\mathrm{i}(q-s)\phi}. \tag{110}$$

We have that

$$P_{\nu}^{q-s}(1) = \begin{cases} 1 & q = s \\ 0 & q \neq s \end{cases}. \tag{111}$$

We then find that

$$Y^{*}_{\nu,q-s}(\mathbf{e}_z) = \begin{cases} \sqrt{\frac{2\nu+1}{4\pi}} & q = s \\ 0 & q \neq s \end{cases}. \tag{112}$$

Substitute (112) and $q = s$ into (109) to find

$$2\sqrt{\pi} \sum_{\nu=|p-r|}^{p+r} \mathrm{i}^{\nu} j_{\nu}(kD) \sqrt{\frac{2\nu+1}{4\pi}} \sqrt{(2r+1)(2\nu+1)(2p+1)} \begin{pmatrix} r & \nu & p \\ 0 & 0 & 0 \end{pmatrix} \begin{pmatrix} r & \nu & p \\ s & 0 & -s \end{pmatrix}. \tag{113}$$

We will now examine what happens when $r \to \infty$. We use the following property of the Wigner 3-j symbols [2]

$$\begin{pmatrix} j_1 & j_2 & j_3 \\ m_1 & m_2 & m_3 \end{pmatrix} = (-1)^{j_1+j_2+j_3} \begin{pmatrix} j_1 & j_3 & j_2 \\ m_1 & m_3 & m_2 \end{pmatrix}. \tag{114}$$

We also make of the following asymptotic form of the Wigner 3-j symbols for $l_1 \ll l_2, l_3$ [2]

$$\begin{pmatrix} l_1 & l_2 & l_3 \\ m_1 & m_2 & m_3 \end{pmatrix} \approx (-1)^{l_3+m_3} \frac{d^{l_1}_{m_1,l_3-l_2}(\theta)}{\sqrt{2l_3+1}}, \tag{115}$$

with $\cos(\theta) = -2m_3/(2l_3+1)$, and with $d^{l_1}_{m_1,l_3-l_2}(\theta)$ Wigner's small d-matrix. We then find the following

$$\begin{pmatrix} p & r & \nu \\ 0 & 0 & 0 \end{pmatrix} \approx (-1)^{p+\nu+r}(-1)^r \frac{d^p_{0,r-\nu}(\frac{\pi}{2})}{\sqrt{2r+1}}. \tag{116}$$

and

$$\begin{pmatrix} r & \nu & p \\ s & 0 & -s \end{pmatrix} \approx (-1)^{\nu} \frac{d^p_{-s,\nu-r}(\frac{\pi}{2})}{\sqrt{2\nu+1}}. \tag{117}$$

We also make use of the large-order approximation of the ordinary Bessel function [3]

$$J_\nu(z) \approx \frac{1}{\sqrt{2\pi\nu}} \left(\frac{ez}{2\nu}\right)^\nu, \tag{118}$$

with z the argument, and ν the order. The spherical Bessel function is defined in terms of the ordinary Bessel function in the following way [3]

$$j_\nu(z) = \sqrt{\frac{\pi}{2z}} J_{\nu+\frac{1}{2}}(z). \tag{119}$$

We then find

$$j_\nu(kD) \approx \frac{1}{\sqrt{2\nu+1}} \frac{1}{\sqrt{2kD}} \left(\frac{ekD}{2\nu+1}\right)^{\nu+\frac{1}{2}}. \tag{120}$$

Substituting all of this into (113) and simplifying, we find

$$\sum_{\nu=|r-p|}^{p+r} \mathrm{i}^\nu \frac{1}{\sqrt{2kD}} \sqrt{2p+1} \left(\frac{ekD}{2\nu+1}\right)^{\nu+\frac{1}{2}} (-1)^p d^p_{0,r-\nu}\left(\frac{\pi}{2}\right) d^p_{-q,\nu-r}\left(\frac{\pi}{2}\right). \tag{121}$$

We estimate this by

$$\sum_{\nu=|r-p|}^{p+r} \frac{1}{\sqrt{2kD}} \sqrt{2p+1} \left(\frac{ekD}{2\nu+1}\right)^{\nu+\frac{1}{2}} |d^p_{0,r-\nu}\left(\frac{\pi}{2}\right)||d^p_{-q,\nu-r}\left(\frac{\pi}{2}\right)|. \tag{122}$$

We have the following constraints on $\nu - r$

$$-p \leq \nu - r \leq p, \tag{123}$$

hence Wigner's small d-matrix can take on only a finite number of values and there must exist an upper bound C_1 such that

$$|d^p_{0,r-\nu}\left(\frac{\pi}{2}\right)||d^p_{-q,\nu-r}\left(\frac{\pi}{2}\right)| < C_1. \tag{124}$$

The terms in (122) decrease so fast that the estimate can be approximated by the term with lowest ν

$$\frac{1}{\sqrt{2kD}}\sqrt{2p+1}\left(\frac{ekD}{2\nu+1}\right)^{r-p+\frac{1}{2}} C_1. \tag{125}$$

It is hence be seen that the terms in the spherical harmonics translation matrix converge super-exponentially for $r \to \infty$.

A.1 Tail of the spherical harmonics expansion of outgoing waves

Consider the definition of the outgoing waves for the individual basis functions and apply a spherical harmonics expansion to the exponential factor

$$\int_S \mathbf{f}_i e^{\mathrm{i}k\hat{\boldsymbol{k}}\cdot(\boldsymbol{r}-\boldsymbol{c}_m)} d\boldsymbol{r} = \int_S \boldsymbol{f}_i \sum_{\nu=0}^{\infty} \mathrm{i}^\nu (2\nu+1) j_\nu(k|\boldsymbol{r}-\boldsymbol{c}_m|) P_\nu\left(\hat{\boldsymbol{k}}\cdot\frac{\boldsymbol{r}-\boldsymbol{c}_m}{|\boldsymbol{r}-\boldsymbol{c}_m|}\right) d\boldsymbol{r}. \tag{126}$$

We have the following estimate for the Legendre polynomial

$$|P_\nu\left(\hat{\boldsymbol{k}}\cdot\frac{\boldsymbol{r}-\boldsymbol{c}_m}{|\boldsymbol{r}-\boldsymbol{c}_m|}\right)| \leq 1 \tag{127}$$

We now estimate the absolute values of the spherical harmonics coefficients

$$\int_S |\boldsymbol{f}_i|(2\nu+1) j_\nu(k|\boldsymbol{r}-\boldsymbol{c}_m|) d\boldsymbol{r}. \tag{128}$$

Applying the large-order approximation to the spherical Bessel function results in

$$\int_S |\boldsymbol{f}_i|\sqrt{2\nu+1}\frac{1}{\sqrt{2k|\boldsymbol{r}-\boldsymbol{c}_m|}}\left(\frac{ek|\boldsymbol{r}-\boldsymbol{c}_m|}{2\nu+1}\right)^{\nu+\frac{1}{2}} d\boldsymbol{r}. \tag{129}$$

It can be seen that this decreases super-exponentially.

References

1. http://en.wikipedia.org/wiki/Spherical_harmonics. Accessed: 2015-06-04.
2. http://en.wikipedia.org/wiki/Wigner_3-j_symbols. Accessed: 2015-06-04.

3. Milton Abramowitz, Irene A Stegun, et al. *Handbook of mathematical functions*, volume 1. Dover New York, 1972.
4. Bradley K Alpert and Vladimir Rokhlin. A fast algorithm for the evaluation of legendre expansions. *SIAM Journal on Scientific and Statistical Computing*, 12(1):158–179, 1991.
5. Constantine A Balanis. *Advanced engineering electromagnetics*, volume 20. Wiley New York, 1989.
6. Cris Cecka and Eric Darve. Fourier-based fast multipole method for the Helmholtz equation. *SIAM Journal on Scientific Computing*, 35(1):A79–A103, 2013.
7. Weng Chew, Mei-Song Tong, et al. *Integral equation methods for electromagnetic and elastic waves*. Morgan & Claypool Publishers, 2008.
8. Weng Cho Chew, Eric Michielssen, Jiming Song, and Jian-Ming Jin. *Fast and efficient algorithms in computational electromagnetics*. Artech House, Inc., 2001.
9. Indranil Chowdhury and Vikram Jandhyala. Integration and interpolation based on fast spherical transforms for the multilevel fast multipole method. *Microwave and Optical Technology Letters*, 48(10):1961–1964, 2006.
10. Barry A Cipra. The best of the 20th century: editors name top 10 algorithms. *SIAM news*, 33(4):1–2, 2000.
11. Ronald Coifman, Vladimir Rokhlin, and Stephen Wandzura. The fast multipole method for the wave equation: A pedestrian prescription. *Antennas and Propagation Magazine, IEEE*, 35(3):7–12, 1993.
12. Tommi J Dufva, Jukka Sarvas, and Johan C-E Sten. Unified derivation of the translational addition theorems for the spherical scalar and vector wave functions. *Progress In Electromagnetics Research B*, 4:79–99, 2008.
13. Thomas F Eibert. A diagonalized multilevel fast multipole method with spherical harmonics expansion of the k-space integrals. *Antennas and Propagation, IEEE Transactions on*, 53(2):814–817, 2005.
14. Zydrunas Gimbutas and Leslie Greengard. A fast and stable method for rotating spherical harmonic expansions. *Journal of Computational Physics*, 228(16):5621–5627, 2009.
15. Leslie Greengard and Vladimir Rokhlin. A fast algorithm for particle simulations. *Journal of computational physics*, 73(2):325–348, 1987.
16. Nail A Gumerov and Ramani Duraiswami. Recursions for the computation of multipole translation and rotation coefficients for the 3-d helmholtz equation. *SIAM Journal on Scientific Computing*, 25(4):1344–1381, 2004.
17. Nail A Gumerov and Ramani Duraiswami. *Fast multipole methods for the Helmholtz equation in three dimensions*. Elsevier, 2005.

18. Nail A Gumerov and Ramani Duraiswami. Fmm accelerated bem for 3d laplace & helmholtz equations. In *Proceedings Int. Conf. on Boundary Element Techniques*, 2006.
19. Nicholas Hale and Alex Townsend. A fast fft-based discrete legendre transform. *arXiv preprint arXiv:1505.00354*, 2015.
20. Michael Larkin Hastriter, Shinichiro Ohnuki, and Weng Cho Chew. Error control of the translation operator in 3d mlfma. *Microwave and Optical Technology Letters*, 37(3):184–188, 2003.
21. George C. Hsiao and Ralph E. Kleinman. Mathematical foundations for error estimation in numerical solutions of integral equations in electromagnetics. 45(3):316–328, 1997.
22. Seppo Järvenpää and Pasi Ylä-Oijala. A global interpolator with low sample rate for multilevel fast multipole algorithm. *Antennas and Propagation, IEEE Transactions on*, 61(3):1291–1300, 2013.
23. Seppo Järvenpää and Pasi Ylä-Oijala. Multilevel fast multipole algorithm with global and local interpolators. *Antennas and Propagation, IEEE Transactions on*, 62(9):4716–4725, 2014.
24. Andreas Kirsch and Frank Hettlich. The mathematical theory of maxwells equations. *Lecture notes*, 2009.
25. Sencer Koc, Jiming Song, and Weng Cho Chew. Error analysis for the numerical evaluation of the diagonal forms of the scalar spherical addition theorem. *SIAM Journal on Numerical Analysis*, 36(3):906–921, 1999.
26. Christian Lessig, Tyler de Witt, and Eugene Fiume. Efficient and accurate rotation of finite spherical harmonics expansions. *Journal of Computational Physics*, 231(2):243–250, 2012.
27. Alexander Nagel, Walter Rudin, et al. Moebius-invariant function spaces on balls and spheres. *Duke Math. J*, 43(4):841–865, 1976.
28. Didier Pinchon and Philip E Hoggan. Rotation matrices for real spherical harmonics: general rotations of atomic orbitals in space-fixed axes. *Journal of Physics A: Mathematical and Theoretical*, 40(7):1597, 2007.
29. Sadavisa M. Rao, Donald R. Wilton, and Allen W. Glisson. Electromagnetic scattering by surfaces of arbitrary shape. 30(3):409–418, 1982.
30. Vladimir Rokhlin and Mark Tygert. Fast algorithms for spherical harmonic expansions. *SIAM Journal on Scientific Computing*, 27(6):1903–1928, 2006.
31. Jukka Sarvas. Performing interpolation and anterpolation entirely by fast Fourier transform in the 3-D multilevel fast multipole algorithm. *SIAM Journal on Numerical Analysis*, 41(6):2180–2196, 2003.

32. JM Song and WC Chew. Error analysis for the truncation of multipole expansion of vector Green's functions. In *Antennas and Propagation Society International Symposium, 1999, IEEE*, volume 1, pages 628–631, 1999.
33. Zhihui Tang, Ramani Duraiswami, and Nail A Gumerov. Fast algorithms to compute matrix-vector products for pascal matrices. 2004.
34. Jun-Sheng Zhao and Weng Cho Chew. Applying matrix rotation to the three-dimensional low-frequency multilevel fast multipole algorithm. *Microwave and Optical Technology Letters*, 26(2):105–110, 2000.